The Spherical Symmetry of the Kilonova AT2017gfo

Master Thesis

Written by:
Albert Bjerregård Sneppen

October 31, 2021

Supervised by:
Darach Watson

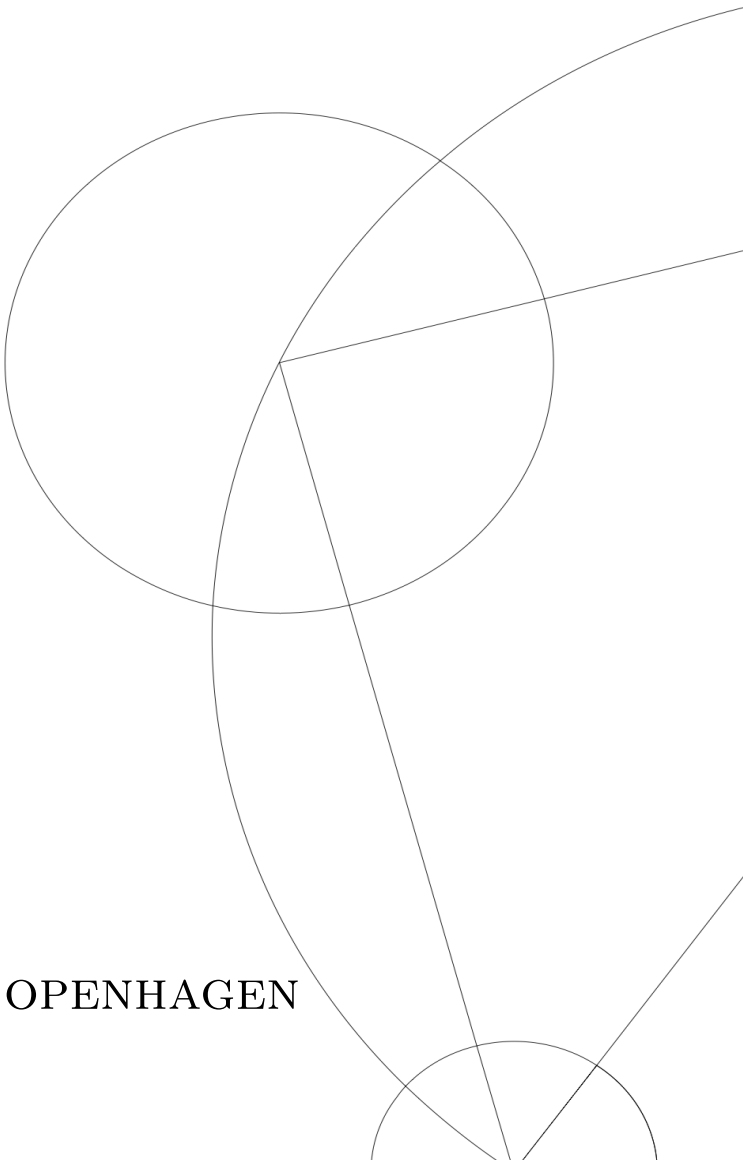

University of Copenhagen

UNIVERSITY OF COPENHAGEN

FACULTY:	Science
INSTITUTE:	Niels Bohr Institute
AUTHOR:	Albert Sneppen
TITLE:	The Spherical Symmetry of the Kilonova AT2017gfo
SUPERVISOR:	Darach Watson
HANDED IN:	31^{st} of October 2021

Acknowledgements

Firstly, I would like to thank my supervisor Darach Watson for the many insightful discussions, for challenging me and for the unyielding enthusiasm which you have shown towards the physics we have shared.

I received a great deal of insight from discussions on the physical processes and hydrodynamical simulations of kilonovae from Ehud Nakar, Andreas Bauswein, Oliver Just, Rubina Kotak and Dovi Poznanski. Further, Radek Wojtak provided useful deliberations on the peculiar velocity modelling of NGC4993 and on the late-universe measurements of the Hubble constant. I also want to express my gratitude for the help given by Rune Thinggaard Hansen on discussions concerning the proper derivation of Doppler corrections over the photospheric surface, for Rasmus Damgaard Nielsen's help in C-code and ideas for computationally speeding-up the calculation of the P Cygni functions, for Caroline Gwynneth Llewellyn's help in proof-reading my manuscripts and Julie Kiel Holm for the confidence, the variable Υ and a variety of discussions on astrophysics.

Lastly, I would like to recognize the friend who keeps reminding me of the value of asking creative questions, reprimanding me for my more uninspired Fourier Transforms and who is always willing to play with physics.

Abstract

The geometry and composition of the astrophysical transients called kilonovae is set by extreme and observationally ill-constrained physics. It requires an understanding of the physics of neutron stars with their incredible gravity, high-density and strong electromagnetic fields. Furthermore, it depends on the the nature of neutrino transport and by the extreme energetics of a putative, potentially powerful and short-lived massive remnant. Additionally, an understanding of kilonovae ejecta is essential in revealing the formation of all the heaviest elements of the periodic table. Despite the unique physical processes worth probing and a multitude of prior analysis, there exists as of yet no tight observational constraints on either the geometry or composition of these extreme explosions.

In this thesis, we determine the first precision measurements of geometry for the only well-studied kilonova to date, AT2017gfo. We will exploit the blackbody nature of the early kilonova spectra and the strong Sr^+ P Cygni absorption-emission feature, which in conjunction constrain the sphericity at multiple epochs by comparing its radial line velocity to its tangential emitting area. Contrary to the typically aspherical ejecta of current hydrodynamical merger models, we show that the kilonova is highly spherical in early epochs. Line shape analysis combined with the known inclination angle of the source independently validate the same sphericity. The highly spherical ejecta not only challenges and constrains future hydrodynamical merger modelling, but it may also imply that kilonovae such as AT2017gfo are precise cosmological probes of distance.

Contents

1 Introduction **1**

1.1 Kilonovae 1

1.2 The origin of the heavy elements 4

1.3 The kilonova AT2017gfo 5
1.4 The H_0 Tension 8
1.5 The paradigm of asphericity 9

2 Methodology **11**
2.1 Expanding Photosphere Method 11
2.1.1 Continuum Emission of AT2017gfo 13
2.1.2 P Cygni Modelling 17
2.1.3 Robustness of the spectral modelling and epoch selection 18
2.1.4 Exploring the posterior landscape with Markov Chain Monto Carlo 19
2.2 Cosmology 21
2.3 Line Asymmetry 24
2.3.1 Constraining a Simulated P Cygni Profile 26

3 Results **28**
3.1 Constraints on Distance 28
3.2 Constraint on inclination angle 31
3.3 Constraint on Sphericity 34
3.3.1 Constraint from Line Shape 35
3.4 Future Constraints on the Hubble Constant 35
3.5 The emergent line; the 0.75μm P Cygni 41
3.6 The Multi-temperature Blackbody 44

4 Discussion **49**
4.1 Limitations of EPM 49
4.1.1 Time Delay 49
4.1.2 Flux Calibration 50
4.1.3 Dilution Factors 51
4.1.4 Line-blending 53
4.1.5 Sr^+ - an accurate indicator of photospheric velocity? 55

4.2 Advantages of EPM for Kilonovae Applications 55
4.3 Potential physical causes of sphericity 57

5 Conclusion **59**

References **61**

1 Introduction

The spectacular gravity, high-density and strong electromagnetic fields of neutron stars make them unique probes of physics in the most extreme of circumstances. Historically, measuring this exotic regime has been difficult, but with the advent of multi-messenger astronomy and the recent detection of merging neutron stars, we can now observationally explore and constrain this physical domain. This open the possibility of understanding the physics of extreme densities and temperatures, creates an entirely independent measurement-tool for cosmological distance and contains the telltale fingerprints of the synthesis of half the heavy elements in the universe.

To examine this extreme domain, we will study the constraints attainable from the spectra of two such merging neutron stars. In Sec 1.1 and 1.2, we will contextualize the unique physical conditions present in such a merger, while deliberating on the theoretical predictions of its geometry in Sec 1.5. In Sec. 2 we will introduce the method of expanding photosphere and the framework of line shapes which we utilize to constrain the geometry of this explosion. We present the constraints these methodologies allow on distance, viewing angle, sphericity and even for cosmological concerns in Sec. 3. Ultimately, these results suggest a remarkably high degree of sphericity in clear contrast to typical hydrodynamical models. Therefore, we discuss the potential biases, limitations and strength of the methodologies applied in Sec. 4. Finally, we reflect on the potential implications and physical interpretations this nearly spherical geometry requires for our understanding of neutron star mergers.

1.1 Kilonovae

When a binary of neutron stars spiral in towards each other and merge, they form a transient astronomical phenomenon, we call a kilonova. In this thesis, we will examine and interpret the structure of such kilonova, but before doing so we must first understand the unique physical conditions present in this merger.

Neutron stars (NS) themselves are a regime of ill-constrained high-energetic physics.

They are believed to be the remnant of massive stars, which throughout their lifetime have sustained themselves in hydrostatic equilibrium by balancing the force of gravity with the pressure provided by the energy of nuclear fusion. However, there is no more binding energy to be gained from fusion after forming Iron, so when an iron-core forms, fusion-processes can only continue in shells around the core. The core itself is held up by electron degeneracy pressure until it reaches the Chandrasekhar mass ($\approx 1.4 M_{\odot}$), whereupon it cannot sustain itself and the process of a core-collapse supernovae begins. The temperature, density and pressure increases as the core collapses, while electron and protons fuse to form now stable neutrons. These get increasingly densely stacked until the neutron degeneracy pressure dominates and a neutron star is born.

The compact object left behind probes a unique and ill-constrained regime of physics. Its density is comparable to that of an atomic nucleus with a mass comparable to the sun but contained within a radial size of around ten kilometers. They must often spin at extreme frequencies up to 10^3 times per second [1], due to the conservation of their much larger progenitor star's angular momentum. They also may have extreme magnetic field strengths up to $10^4 - 10^{11}$ T [2], as they inherit the magnetic field of their progenitor star within a far smaller volume.

When two such compact objects in close proximity rotate around their common center of mass, they emit a gravitational wave. As the gravitational radiation carries energy away, the two objects rapidly rotate and spiral inward, moving at a fraction of the speed of light until they ultimately coalesce into a single object. In the brief moments before collision the large gravitational tidal forces may liberate matter in the plane of the binary. This is followed by a compression-induced heating at the interface of the merging neutron stars which may eject additional matter [3]. The relative and total contributions of each of these two "dynamical" mechanisms depends sensitively on the neutron star's equation of state and the masses of each of the neutron stars.

The properties of this ejecta may also depend on the energetics added from the forming central remnant, while the ultimate fate of this remnant itself depends sensitively on the total mass of the neutron star binary. If the total mass exceeds a

still ill-constrained threshold mass of $\approx 2.6 - 3.9 M_{\odot}$ (set by the unknown NS equation of state), the remnant collapses to a black hole on a time-scale of milliseconds or less. Lighter mergers would result in the formation of a rapidly-spinning neutron star remnant, either (although unlikely) small enough to be stable itself or (more typically) temporarily supported by its rotation [3]. Immediately surrounding this remnant could be a recently formed accretion disk from tidally displaced matter. This central neutron star remnant, if it's sustained for longer than 50 ms, would even contribute a high level of neutrino irradiation, which could blow out additional mass from the accretion disk [4]. Numerical simulations suggest the mass ejected in this "disk wind" may be comparable to or larger than what is expected from the tidal or shock-heating ejection process described on the dynamical time of the merger. However, due to the later process of ejection, this matter would necessarily be deeper within the substructures of the expanding ejecta. Even more exotic physical processes have also been suggested: Notably, the strong magnetic field of a NS remnant may enhance other ejection processes along the open magnetic field lines and produce a so-called "magnetar-wind" [5]. Such process could potentially be responsible for the fastest ejecta of such kilonovae [6]. A summary of the different ejection channels discussed with their associated velocities and total masses is schematically illustrated in Fig. 1.

Regardless of the many suggested physical processes invoked to understand the ejecta, there are some generic features universally expected. The liberated ejecta matter expands rapidly moving typically at velocities $0.1 - 0.3c$ with a total dynamical ejecta masses in the range $10^{-4} - 10^{-2} M_{\odot}$ [7]. The ejecta has a unique composition, as it is very neutron-rich and correspondingly has a small electron fraction, typically labelled $Y_e = \frac{n_p}{n_n + n_p}$ (here n_p and n_n indicates the densities of protons and neutrons). Typical stellar material usually has more protons than neutrons ($Y_e > 0.5$), while kilonovae have an excess of neutrons ($Y_e < 0.5$). Understanding this highly neutron-rich ejecta is an active topic of research, not only because it sheds light on the illusive high-energy regime of neutron stars and their merger processes, but also because it is a crucial site for the synthesis of heavy elements.

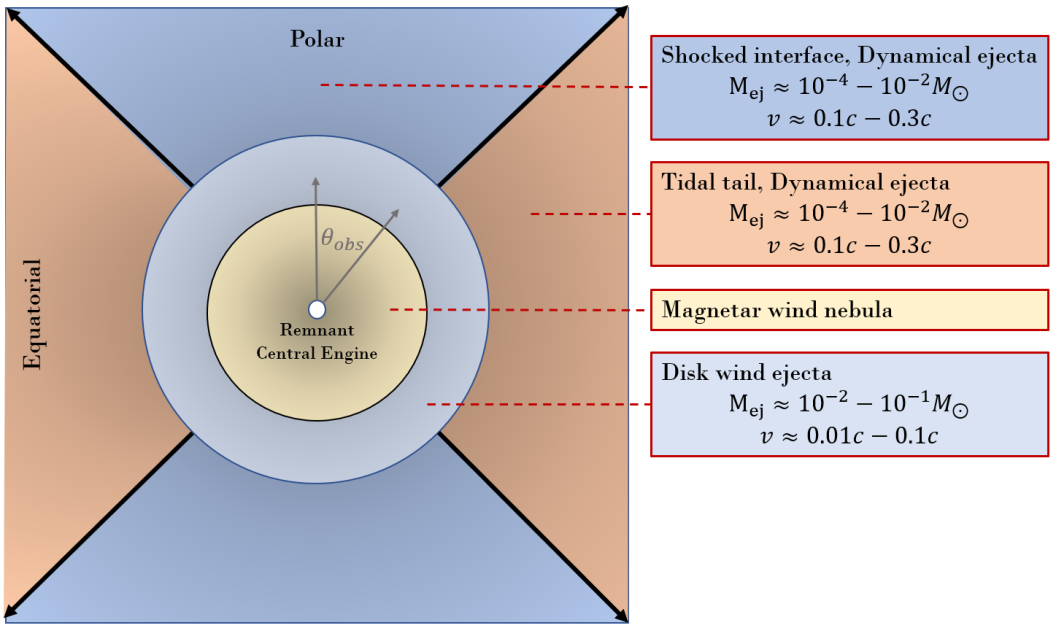

Figure 1: **Different ejecta-components from a neutron star merger with potential dependence on viewing angle, θ_{obs} adapted from Metzger 2019 [3]**. The shocked interface ejecta, predominantly in polar directions, may be relatively neutron-poor. The tidal tail, predominantly in the equatorial plane, is highly neutron-rich. The later time ejection from accretion disk outflows may emerge more isotropically. Energy input from the central magnetar remnant or accreting black hole may provide additional mass ejection and luminosity.

1.2 The origin of the heavy elements

Elements are synthesized through a wide range of processes: the nucleosynthesis in the cores of stars producing elements lighter than iron, while slow and rapid neutron capture processes can produce the heavier elements of the periodic table. The slow neutron capture process (s-process) is when a nucleus captures a neutron, thereby forming a potentially unstable isotope, which may beta-decay and thus slowly increase its atomic number. For instance iron seeds may fuse with neutrons in relatively low neutron-flux environments like that present in stars on the asymptotic giant branch. In contrast, in the neutron-rich environments (such as in core-collapse supernovae or

in the kilonova ejecta) a rapid flux of neutrons, may add to the atom on time-scales shorter than the beta-decay of formed elements. Only these sites of rapid neutron capture (r-process) can produce the heaviest elements of the periodic table such as gold, radon or uranium.

Core-collapse supernovae were historically believed to be the predominant source of r-process elements. However, it is questionable whether they can account for the total abundance of heavier elements observed. In contrast, recent numerical and theoretical considerations indicate that neutron star mergers are likely a major and predominant source of r-process elements in the late universe [8, 9]. The different physical ejection mechanisms of kilonovae all produce unique elementary abundances. For instance the tidally disrupted material will unbind highly neutron-rich matter ($Y_e < 0.30$) capable of forming heavy r-process nuclei such as Lanthanides. In contrast, the expectation is that processes irradiated by a strong flux of neutrinos from the NS remnant will have a higher electron fraction ($Y_e > 0.30$) which in turn produces only lighter r-process elements. Ultimately, understanding the physical conditions present in the kilonova sheds new light on the origin of these heaviest of elements.

The radioactive decay of r-process elements synthesized during the merger and a potentially (although speculatively) central engine heats the ejecta from within [3]. As a consequence the kilonova is a luminous transient, peaking with a luminosity comparable to billions of solar mass stars, but fading within a time-scale of the order of a few days. This light, and the spectral signatures it may contain is the central focus of this thesis.

1.3 The kilonova AT2017gfo

On August 17th 2017, a simultaneous detection of gravitational wave (GW) signal and electromagnetic radiation heralded the beginning of the era of multi-messenger astronomy. Firstly, the Advanced LIGO and Virgo interferometers detected a gravitational wave signal from the inspiral and merger of a binary of compact object, which was

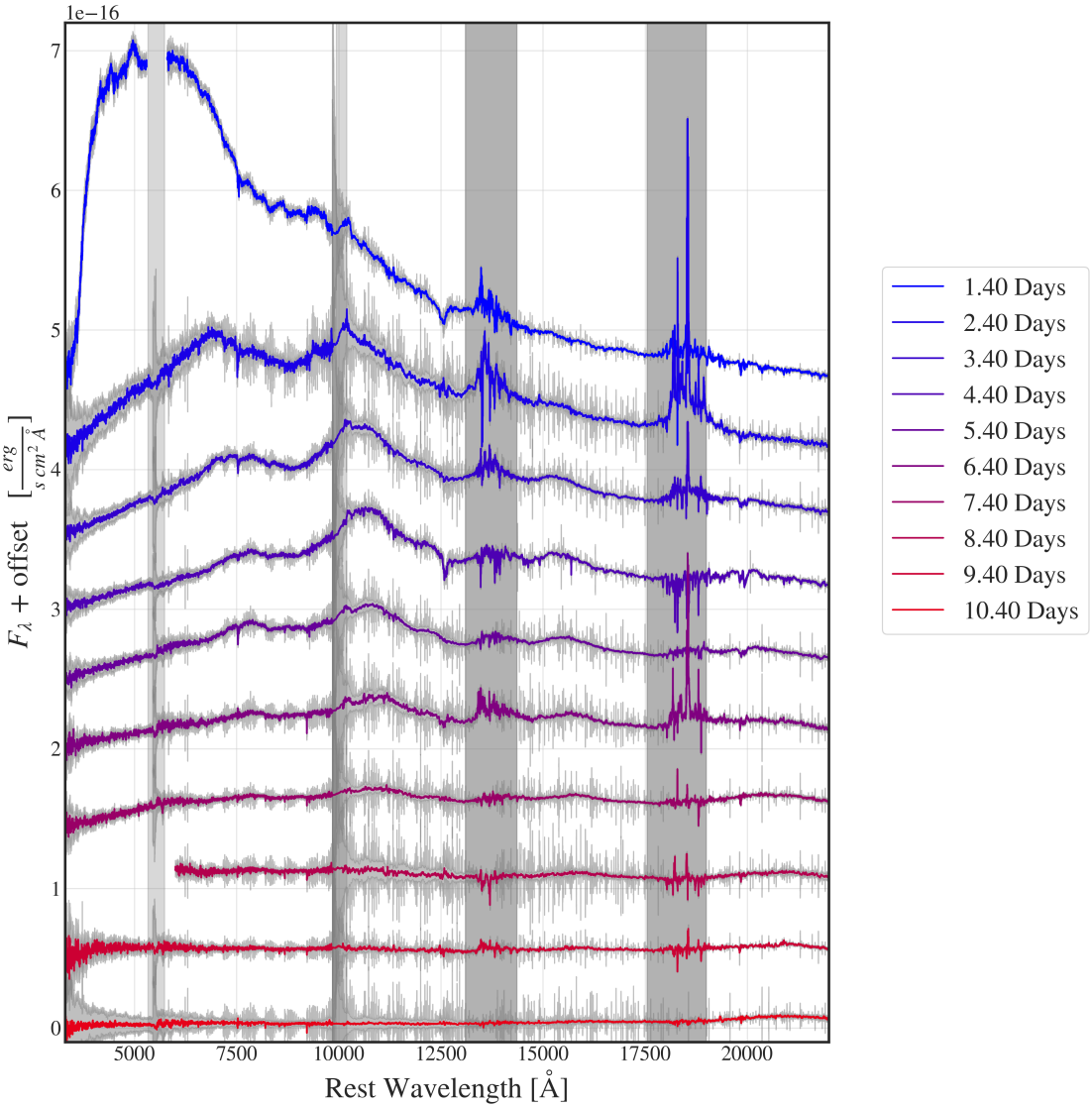

Figure 2: **Spectrum of the kilonova AT2017gfo across ultraviolet, optical and near-infrared from X-shooter spectrograph for each epoch from 1.4 (blue) to 10.4 (red) days after neutron star merger GW170817**. Dark shaded bars indicate telluric regions; Light shaded bars indicate overlapping noisy regions between the UVB, VIS and NIR arms. Spectral features in the shaded regions are excluded from the analysis.

designated GW170817 [10]. The two component masses were determined to be in the range $1.17-1.60 M_{\odot}$ implying that they were neutron stars, but that their ultimate coalescence would form a black hole. Secondly, a near-simultaneous temporal and spatially consistent short gamma-ray burst GRB170817A was detected [11]. Thirdly, a transient kilonova (designated AT2017gfo) was observed in the elliptical galaxy NGC4993 within the 31 deg^2 area indicated by the GW signal [11]. The object was measured across a wide range of observatories covering wavelengths from radio to X-rays. These electromagnetic observations were inconsistent with any previously observed astrophysical transient with a uniquely rapid rise and subsequent drop in flux, a fast evolution in color from ultraviolet to infrared over a few days, and an initially nearly featureless smooth spectra dominated by a blackbody continuum [12]. However, this transient was remarkably consistent with prior theoretical models for thermal emission from a kilonova. One notable exception from prior models is that the total amount of ejected mass, $M_{ej} > 0.02 M_{\odot}$, far exceeds predicted dynamical ejections from virtually any merger simulations. This provides preliminary indications that more exotic ejection mechanisms or energy ejections may be required.

Among many observations the series of spectra of AT2017gfo taken with the medium resolution, ultraviolet (320 nm) to near-infrared (2.480 nm) spectrograph X-shooter, mounted at the Very Large Telescope at the European Southern Observatory provides the most detailed information of any kilonova to date [13, 14]. The daily spectra taken between 1.4 to 10.4 days after the event [see Fig. 2] yields a temporal evolution of continuum, emission and absorption features. This unprecedented and detailed spectral decomposition opens for a wealth of studies from examining neutron-stars [15], neutron-star mergers, the rapidly expanding ejecta of a kilonova [14], the formation of r-process elements [16] to constraining the expansion rate of the universe.

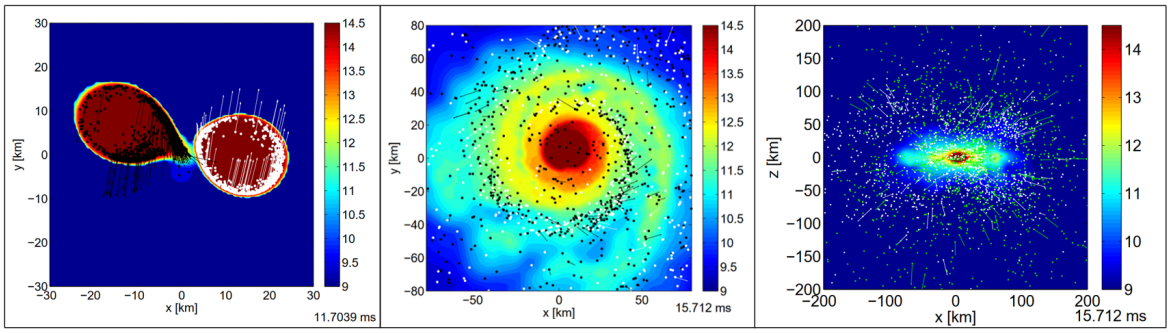

Figure 3: **Density distributions from hydrodynamical merger model of Bauswein 2013 [8].** The rest-mass density (logarithmically plotted in $\frac{g}{cm^3}$) in the equatorial plane (left and middle for two different temporal snapshots) and the plane perpendicular to the orbital plane (right) from hydrodynamical merger model from Fig. 4 and 5 in [8]. The large angular momenta produces an asymmetry between polar and equatorial ejection.

1.4 The H_0 Tension

A noteworthy potential of kilonovae analysis is the novel constraints they may shed on the expansion rate of the universe, the so-called Hubble Constant, H_0. A precise understanding of H_0, is a critical measurement driving the study of cosmology. However, with the growing precision of cosmological studies has followed an increasing tension, currently significant at 5σ, between measurements of the H_0 from late-Universe methods [17] and indirect probes from the early-Universe [18]. If true, this would suggest the standard cosmological paradigm, ΛCDM, cannot simultaneously fit observations at all redshifts, which necessitates modifications to the cosmological model or to the physics of the early-Universe.

Alternatively, ΛCDM paradigm may still be valid, if unaccounted systematic effects have biased the inferred H_0 from either framework. For the local H_0-constraints, which utilizes Cepheid and SN observation, this includes (but is not limited to) issues in SNIa dust extinction modelling [19, 20], Cepheid metallicity correction [21], host-galaxy properties [22] and different population of SNIa at low-z and high-z [23, 24]. Given

the many potential systematics, independent measurements of the Hubble constant on local cosmic distance scales provide crucial evidence on the interpretation of the H_0 divergence.

A multitude of independent probes have been developed, including notable time delays of gravitationally lensed variable source [25, 26], megamaser distance measurements [27] and the gravitational wave standard siren [10]. However, any conclusive interpretation remains illusive due to the as-of-yet limited statistics and modelling uncertainties for all these methodologies. However, the rapid growth in gravitational wave sensitivity and the promising abundance of optical counterparts suggests tights 1-2 % statistical constraints may soon be attainable [28]. Indeed, the first gravitational wave detection of a binary neutron-star merger, GW170817 [10], and the ensuing optical transient kilonova, AT2017gfo [11], has already provided several promising estimators of H_0 [29, 30]. The tightest current H_0-constraint are from combining very-long-baseline interferometry constraints with the GW siren yielding fractional uncertainty of 7% [31].

However, as we will show in this thesis, the clear blackbody-continuum of early spectra may make AT2017gfo and similar kilonovae excellent high-precision cosmological probes if we can determine the geometry of the expanding ejecta.

1.5 The paradigm of asphericity

The kilonovas geometry and composition remains unknown and depends, among other things, on the equation of state of ultra-dense matter, neutrino transport, and the properties of a proposed powerful and short-lived massive neutron star post-merger. Current hydrodynamical merger models typically show aspherical ejecta both in terms of density, elementary abundances and opacity [8, 32, 33, 34].

The density distribution is typically aspherical due to the large angular momentum of the spiralling neutron stars (as illustrated in the hydrodynamical merger simulations of Fig. 3). Near collision the large tidal components are expected to liberate matter along the plane of the merger [8], which would create an oblate density dis-

tribution. Additional material at the contact interface between the merging neutron stars is squeezed out by hydrodynamic forces [32, 35], ejecting shock-heated matter in a broad range of angular directions. Furthermore, the post-merger remnant, either a massive neutron star or a black hole, may further impact the energetics and mass ejection. With magneto-hydrodynamical processes, such as magnetic winding and magneto-rotational instability governing the evolution of the disk and setting the mass ejection on a timescale of seconds after the merger [36]. A large injection of energy, potentially released from the rotational energy of the systemafter the merger could make the density distribution more spherical by puffing it up [33]. However, in this unconstrained domain of an unknown neutron star equations of state, instabilities of turbulent magneto-hydrodynamics and potential energetics of central remnant, the ultimate geometry of kilonovas remain theoretically completely ill-constrained.

Furthermore, as discussed in Sec. 1.2 a pole-to-equator variation of the electron fraction, Y_e, is expected due to the more pronounced neutrino emission towards the poles [37, 38, 39]. Low-Y_e disk ejecta contribute significant amounts of equatorial outflows, while neutrino-driven winds dominated by lower opacity, high-Y_e matter are ejected preferentially towards the poles [40, 41, 42]. This should lead to an elementary abundance, which is not spherical. However, all current predictions of differences between the ejected equatorial and polar matter compositions are sensitive to neutrino physics and neutrino flavor conversion processes which still is poorly understood [43].

While a reasonable degree of sphericity in density or composition is in principle compatible with some current models, it is far from a generic and expected outcome. However, as we will show in this thesis, we can provide the first tight observational constraints on AT2017gfo's sphericity at multiple epochs. We will show, that contrary to the wide diversity of hydrodynamical merger models, the kilonova is highly spherical.

2 Methodology

2.1 Expanding Photosphere Method

The expanding photosphere method (EPM) is a tool for measuring the luminosity distance, D_L, to objects with large amounts of ejected material [44]. While the methodology was first developed for examining core-collapse supernovae, in this thesis we show that kilonova are apt terrain for this kind of analysis. Early follow-up spectroscopy of kilonovae yield constraints on continuum and lines, while the gravitational wave and gamma-ray signals provide independent constraints on the time and orientation of the merger, and the environments around kilonovae are less obscured than their dustier supernova counterparts [45]. Ultimately, these factors allow EPM to provide precise and internally consistent estimates on the distance to AT2017gfo.

EPM is based on a simplified model with a four key assumptions:

1. The photosphere radiates as a blackbody and therefore a specific luminosity, L_λ with a characteristic temperature. As discussed in § 2.1.1 the blackbody continuum approximation proves accurate in early epochs, but the relative size of emission and absorption components increases with time.

2. The expansion of the ejected material is spherically symmetric.

3. The ejecta is expanding homologously, which means any particular layer, R, in the ejecta has a constant expansion velocity, v_R. Thus, $R(t) = v_R \cdot (t - t_e)$. Here $t - t_e$ is the time since the initial moment of explosion. Simulation of ejecta of kilonova explosions suggest homologous expansion are expected on the timescale investigated in this analysis [33].

4. The ejecta is optically thick, ie. there exists a layer, termed "the photosphere", where the optical depth $\tau_\lambda \approx 1$. During the expansion the outer layers become optically thin so the location of the photosphere moves inwards in the ejecta.

Therefore the velocity, v_{phot}, is decreasing with time, but is at any given epoch well-constrained by fitting the P-Cygni feature discussed in § 2.1.2.

Thus, at any point in time the photosphere size directly follows from the expansion velocity and the time since explosion:

$$R_{phot} = v_{phot}(t - t_e) \tag{1}$$

The overall luminosity of a spherical blackbody is $L_\lambda^{\rm BB} = 4\pi R_{\rm phot}^2 \pi B(\lambda, T_{\rm eff})\delta^{-2}$, where $B(\lambda, T_{\rm eff})$ is the Planck function and δ is the relativistic Doppler correction [46]. Due to the rapid velocity of expansion, we must be careful when comparing our observed frame of references with the rapidly expanding frame of the ejecta, so we correct for aberration by including the relativistic Doppler correction as we discuss in Sec 2.1.1. The specific total luminosity inferred from observations is $L_\lambda^{\rm obs} = 4\pi D_L^2 F_\lambda$, where F_λ is the wavelength specific flux. Equating the blackbody-inferred and observed luminosities yields a relation for the angular size, θ, of the ejecta:

$$\theta = \frac{2R_{\rm phot}}{D_\theta} = (1+z)^2 \frac{2R_{\rm phot}}{D_L} = 2(1+z)^2 \sqrt{\frac{F_\lambda \delta^2}{\pi B(\lambda, T_{\rm eff})}} \tag{2}$$

Here, D_θ is the angular diameter distance which is converted to luminosity distance using $D_\theta(1+z)^2 = D_L$. Given the angular size and physical extent of the photosphere we deduce the luminosity distance [47]:

$$D_L = (1+z)^2 \frac{2R_{phot}}{\theta} = R_{phot} \sqrt{\frac{\pi B_\lambda(T_{\rm eff})}{F_\lambda \delta^2}} \tag{3}$$

Thus, using the blackbody temperature, the inferred ejecta velocity from the P-Cygni profile and the observed flux, we now have an estimate of the luminosity distance. Crucially, this estimate requires no calibration with known distances and remains entirely independent of the cosmic distance ladder.

Conversely, comparing this EPM distance estimate with any previous inferred distances provides an estimate of the emitting cross-sectional area. Converting the cross-sectional area into a single cross-sectional velocity requires an assumption of axial

symmetry. Given the close to polar inclination inferred from the radio measurements of the jet [48], this corresponds to an assumption of cylindrical symmetry in the plane of the disk. The slight difference between exactly polar and the VLBI inclination constraints yield less than 1 percent variation in inferred cross-sectional area and, while we account for this effect in the cross-section, it is inconsequential to the constraints presented in this thesis. An equivalent way of phrasing this, as illustrated in Fig. 4, is that the overall luminosity is set by the cross-sectional radius (i.e. the perpendicular velocity, $v_\perp$), while the main constraint on $v_{\rm phot}$ is derived from the absorption feature (i.e. the velocity of the photosphere along the line-of-sight, $v_\parallel$). By assuming H_0 and identifying the redshift to NGC4993, we can compare the line-of-sight and orthogonal velocities. We define the zero-centered asymmetry index:

$$\Upsilon = \frac{v_\perp - v_\parallel}{v_\perp + v_\parallel} \tag{4}$$

Here $\Upsilon < 0$ would be a prolate expansion, corresponding to lower velocities in the plane of the binary than along the jet. This comparison does not probe the asymmetry of the mass distribution's deeper substructures - it only constrains the asymmetry of the ejecta photosphere - and naturally cannot probe the unobserved nebular phase. Fortunately, in applying kilonovae to measure cosmological distances or in comparisons with hydrodynamical merger-models constraining sphericity in the photospheric phase is sufficient.

2.1.1 Continuum Emission of AT2017gfo

A blackbody is an ideal surface, which absorbs all incident light, while being a perfect and diffuse emitter. Given these assumptions, the specific luminosity of the photosphere is set by its radius R_{phot} and the Planck function $B_\lambda(T) = \frac{2hc^2}{\lambda^5}\frac{1}{e^{\frac{hc}{k_b T\lambda}}-1}$ with a temperature, T:

$$L_\lambda = 4\pi R_{phot}^2 \pi B_\lambda(T) \tag{5}$$

Previous studies have established that the earliest epochs of AT2017gfo are well-approximated by a blackbody spectrum [49, 50] with complex emission and absorption-

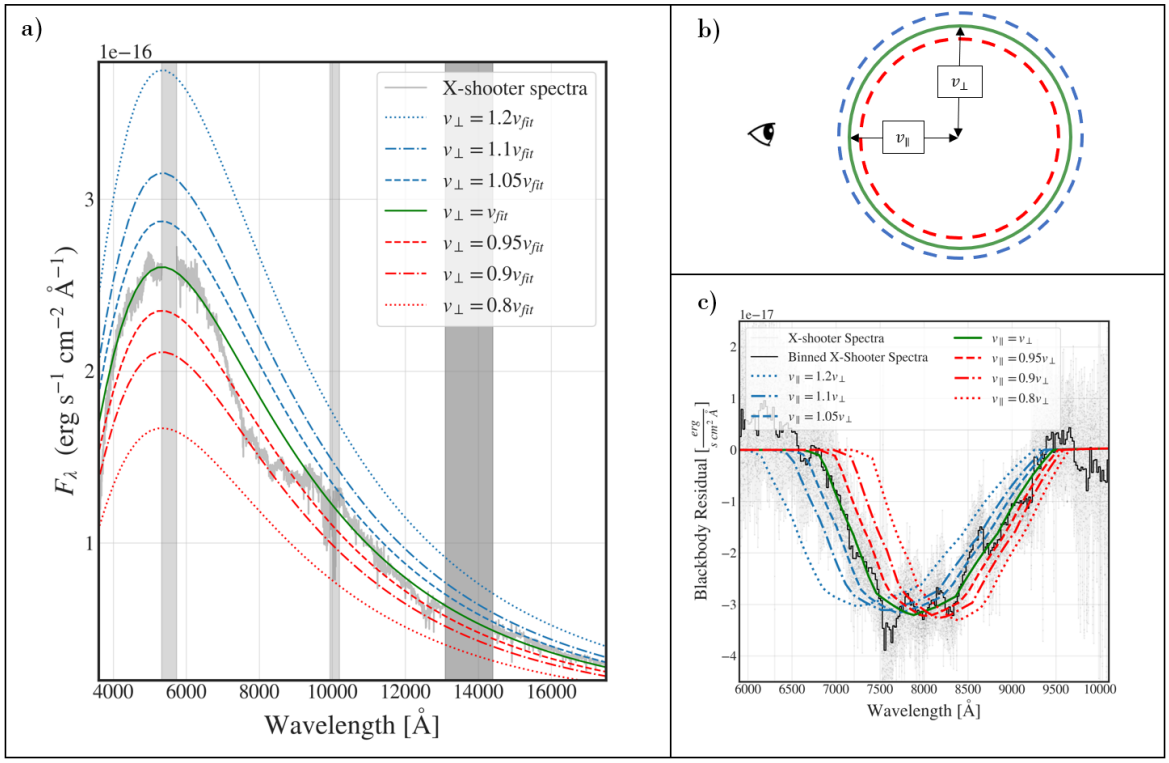

Figure 4: **Illustration of the spectral expanding atmospheres method for the kilonova AT2017gfo.** a) Epoch 1 X-shooter spectrum with overlayed blackbody fits. The normalisation for each blackbody is set by the cross-sectional radius, which requires an *a priori* distance (here assuming the cosmological parameters from the *Planck* mission and the peculiar velocity of the host galaxy, NGC4993) and cross-sectional velocity, $v_\perp$. Smaller (red), equal (green), or greater (blue) values of $v_\perp$ are shown, in comparison to the best-fit velocity, $v_{\rm fit}$. b) Illustration of $v_\parallel$ and $v_\perp$ which are respectively set by the P Cygni absorption feature and the blackbody normalisation. c) Zoom in of the Sr II absorption component residual from subtracting the X-shooter epoch 1 spectrum with the blackbody continuum fit. The P Cygni profiles for $v_\parallel$ smaller (red), equal (green), or greater (blue) than $v_{\rm fit}$ are overlaid. The photospheric velocity $v_{\rm phot}$ and the maximum ejecta velocity $v_{\rm max}$ are shifted coherently. The continuum measurement and absorption line fit yield velocities in tight agreement.

features increasing in magnitude at later times. The main deviations from the blackbody are a few separate emission components. The first, is an increasing excess of radiation at 1μm with two broad absorption features at approximately 350 nm and 810 nm. These spectral components are consistent with the spectral lines of Strontium, further discussed in § 2.1.2. The second is a small excess of emission at wavelengths of around 1.6μm and 2μm increasing in relative strength across the epochs. We model these emission components as Gaussian emission lines to avoid biasing the overall continuum fit (similar to the established approach in [16]). We do not interpret these lines, as the origin of these spectral features remains unresolved. For even later epochs several additional emission components are emergent with a notable potential P-cygni profile observed at around 1.35μm observed in the HST spectra of the 4th day. However, this feature is obscured within the telluric region of the X-shooter data, so its prominence does not influence this analysis. Importantly, these uninterpreted absorption and emission components increase relative to the continuum across the epochs. Therefore, while the continuum emission for the earliest epochs are largely independent of these spectral components, the modelling for later epochs requires constraint on their prominence and multitude. Furthermore, given the wealth of spectral information hiding in these lines, future work should examine and constrain their physical origin.

Note, due to the rapid expansion of the photosphere we must include corrections for the relativistic Doppler effect. The ratio between observed (ν_{obs}) and emitted (ν_{emi}) frequency is set by the velocity of expanding photosphere β, the relativistic Lorentz factor γ and the angle between the observer and the direction of motion, θ [46]:

$$\nu_{\rm obs} = \nu_{\rm emi} \frac{1}{\gamma(1 - \beta cos(\theta))} = \delta(\theta) \cdot \nu_{\rm emi} \tag{6}$$

The coherent shift of all frequencies, scales the inferred blackbody temperature by $T_{\rm eff} = \delta(\theta) T_{\rm emi}$. However, these relativistic corrections also vary time ($dt = dt_{\rm emi}/\delta(\theta)$), the solid angle ($d\Omega = d\Omega_{\rm emi}/\delta(\theta)^2$) and in extension the specific luminosity ($I_\lambda = I_{\lambda,{\rm emi}}\delta(\theta)^5$) between different frames of reference. Integrating the specific luminosity over all wavelengths yields the bolometric luminosity which scales as $I = I_{\rm emi}\delta^4$. While

further details on the relativistic corrections can be found in [46], the emergent picture is one of increasing complexity in the relationship between observed luminosity, area and effective temperature between different frames of reference.

Further complications emerge as the photosphere expands spherically symmetrically, so θ ranges from head-on ($\theta = 0$) to orthogonal motion $\theta = \pi/2$ when viewing different portions of the ejecta. As the magnitude of the Doppler shift of frequencies depends on the viewing angle θ, the blackbody spectrum is blueshifted incoherently for different surface-elements and any exact analytical estimate should convolve an underlying blackbody-spectrum with the distribution of area-weighted Doppler-shift (see Sec. 3.6). However, the difference between shifting by the average blueshift and convolving the blackbody spectrum over an area-weighted distribution of blueshifts is small for the mildly relativistic velocities observed for the photosphere. Indeed, the simplifying approximation of estimating an average Doppler-correction yields consistent results across the first epochs. As the photosphere is optically thick the redshifted ejecta (ie. $\theta > \pi/2$) is occulted. Integrating over the visible photosphere yields the average Doppler correction to the blackbody temperature:

$$\delta = \frac{1}{\gamma} \int \frac{1}{1 - \beta \cos(\theta)} dA = \frac{1}{\gamma} \int_0^{\frac{\pi}{2}} \frac{1}{1 - \beta \cos(\theta)} 2 \sin(\theta) \cos(\theta) d\theta \tag{7}$$

For this analysis, the crucial aspect is that the luminosity of the blackbody observed constrains the cross-sectional area (the solid angle of the photosphere) in our frame of reference. In contrast, the constraints on R_{ph} derived from the line profile represents the physical size of the ejecta. Therefore to compute the emitting area in our frame (ie. to include the effect of aberration when comparing the two velocity constraints), we must decrease the cross-sectional area inferred from the line by δ^2 or correspondingly increase the solid angle inferred in our reference frame by δ^2 to match the kilonova reference frame. A more detailed discussion on the relativistic Doppler correction for a spherical, relativistic and optically thick expanding atmosphere can be found in [51].

2.1.2 P Cygni Modelling

The deviation from the blackbody is mainly characterised by broad absorption features with widths of around 0.2c [50]. The two largest absorption components detected are at around 350 and 810 nm and likely due to strontium (Sr) in the ejecta [16]. Of these the ultraviolet absorption feature is not well-constrained as it lies near the edge of the sensitivity limit, while the optical component is well described by a P-Cygni profile.

The P-Cygni profile is characteristic of expanding envelopes where the same spectral line yields both an emission peak near the rest wavelength and a blueshifted absorption feature [52], as illustrated in Fig. 5. The peak is formed by true emission or by scattering into the line of sight, while absorption is due to scattering of photospheric photons emitted towards the observer out of the line of sight. As the latter is in the front of the ejecta this component is blueshifted. The P-Cygni profile is characterised by several properties of the kilonova atmosphere. The optical depth determines the strength of absorption and emission, while the velocity of the ejecta sets the wavelength of the absorption minimum. For this analysis we use the implementation of the P Cygni profile in the Elementary Supernova [https://github.com/unoebauer/public-astro-tools], where the profile is expressed in terms of the rest wavelength, λ_0, the line optical depth, τ, a scaling velocities for the velocity dependence of τ, v_e, the photospheric velocity, v_{phot} and the maximum ejecta velocity, v_{max}. Furthermore, this implementation does not include the relative population of the states in the transition (ie. the source function), so we include a parameter describing the enhancement/suppression of the P Cygni emission.

Following the prescription of [16] the relevant permitted lines are from the SrII $4p^6 4d$ metastable state which has strong resonance lines at $1,032.7$ nm, $1,091.5$ nm and $1,003.7$ nm. These lines are modelled using the same P Cygni profile prescription, with the relative strengths of each of the lines set by the local thermodynamic equilibrium relation.

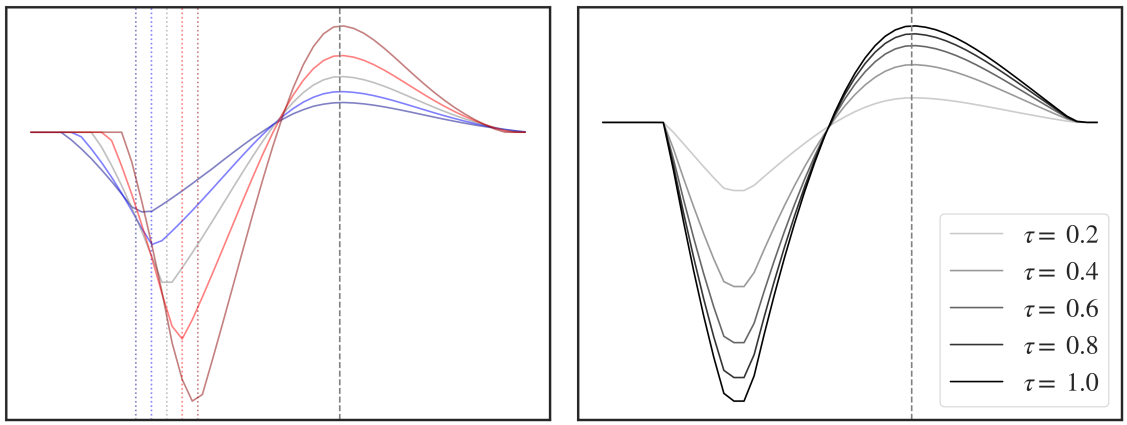

Figure 5: **Example P cygni profiles, which illustrate the evolution of the profile with varying ejecta velocity (left) and varying optical depths (right).** The grey dashed vertical line indicates the rest wavelength of the emitting line. The dotted vertical lines represents this wavelength blueshifted by the photospheric velocity, which for unsaturated lines follows the valley of the absorption profile.

2.1.3 Robustness of the spectral modelling and epoch selection

As mentioned previously, for later epochs, several complex components emerge, including the increasing prominence of the emission component of the $\sim 1\,\mu$m Sr^+ features, an emission feature at $\sim$1.4μm, clearly observed in the *Hubble Space Telescope* spectra from the 5th and 10th days post-merger[53], a P Cygni feature from at least the fourth day onwards at $\sim$0.75μm, and an emission component at $\sim$1.2μm from at least the 5th day onwards. While the models for the earliest epochs are largely independent of these additional spectral components, the modelling for later epochs is increasingly affected by whether and how these features are accounted for. We show in Fig. 6 the effect of including components in the modelling, or excluding spectral regions containing these components, to illustrate the sensitivity of the models to these effects. We still get agreement on the distances to within 10% in all of the first five epochs, regardless of whether we include these components or not. More sophisticated modelling would almost certainly yield much better constraints. However, we use this analysis to show

the robustness of our conclusions for the first two epochs. We base our analysis in this thesis on these two epochs for this reason.

2.1.4 Exploring the posterior landscape with Markov Chain Monto Carlo

Constraining the continuum blackbody, the many parameters describing the P Cygni and any nuisance parameters of the emergent emission lines requires exploring a high-dimensional, complex and covariant parameter-space. While minima of a likelihood function can quickly yield best-fit parameters using a simple numerical method such as Nelder-Mead, we instead choose the more robust (but computationally expensive) method of sampling the posterior probability with Markov Chain Monto Carlo. This is favourable for our analysis as 1) long chains of independent walkers decrease the probability of being dominated by local minima and 2) it provides robust errors associated with each parameter.

We will assume flat priors on all parameters and sample the posterior probability distributions with emcee [54] using the fitting framework LMFIT [55]. When reported the best-fit values are medians of the marginalized posterior probability distribution, while the uncertainties are from the 16th and 84th percentiles.

To constrain the parameters, we run a large ensemble of walkers over a large number of discrete steps in the posterior landscape with specifically a 100 walkers each sampling 10.000 steps within the posterior parameter-landscape of each spectrum. Thus, our walkers probe over many auto-correlation lengths, ensuring the posterior landscape is well-sampled as illustrated for the full model for Epoch 1 (see Fig. 7). We note allthough several non-trivial degeneracies exist between parameters, the posterior distribution is convex with well-centered peaks of the distributions. In the Appendix we provide the sampled distribution for later epochs.

Notable, the desired dense sampling required for exploring a high-dimensional parameter landscape is not computational feasible with the standard P Cygni profile codes. Therefore, we have developed a significantly faster version of the Elementary

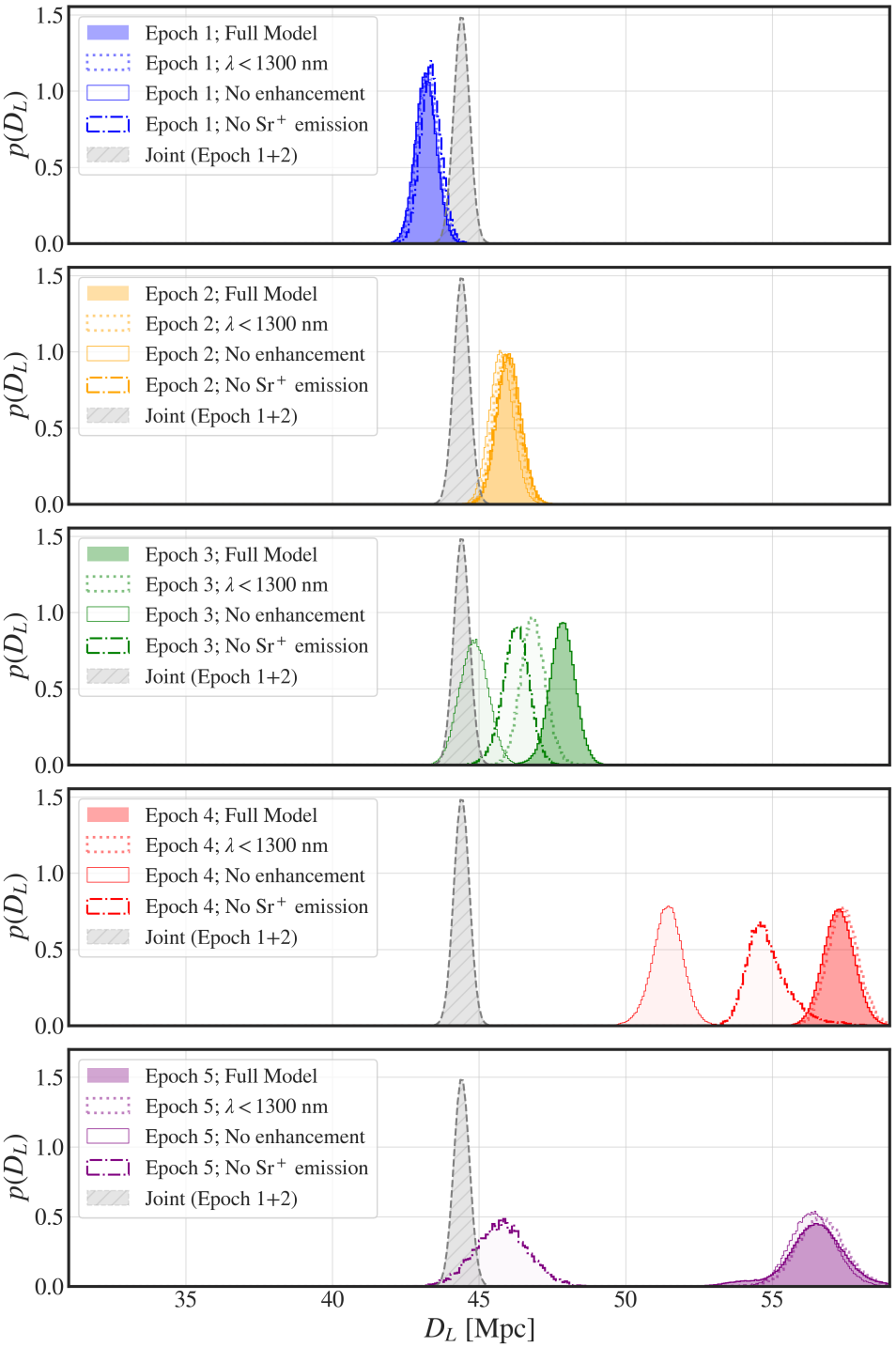

Figure 6: (Continued on the following page.)

Figure 6: **Posterior probability distributions of the luminosity distance to the kilonova AT2017gfo from epochs 1–5.** Our distance estimates based on the kilonova EPM for the spectra obtained at 1.43, 2.42, 3.41, 4.40 and 5.40 days are shown in blue, yellow, green, red, and purple histograms respectively. Filled histograms represent the full model including the blackbody continuum, Sr^+ P Cygni, and two NIR Gaussian emission lines. Dotted histograms indicate constraints from excluding all data with wavelengths longer than 1300 nm, showing that the inclusion of the NIR Gaussian emission features do not bias the full model significantly. The opaque and dash-dotted histograms are for fits which do not include a parameter for enhancement of the emission or altogether excluding the parts of the spectra with the Sr^+ emission line. Distances derived from every epoch are consistent with the distances inferred from the GW standard siren plus VLBI constraints [31], but only the data from epochs 1 and 2 provide robust, tight statistical uncertainties, with no large systematic variation between different models for emission components.

Supernova code, which is mathematically identical, but uses vectorization to quickly computationally parallelise over wavelengths and utilises a Numba-compiler to translate Python functions to optimized machine code. Thus, all the slowest computations now reside within pre-compiled C-functions. The ultimate gain is a overall computational speed-up which decreases the run-time by a factor of approximately 200. This not only permits a dense and rigorously exploration of posterior parameter-landscapes, it also opens the possibility for developing more sophisticated and computationally heavy models, including the ellipsoidal expanding atmosphere discussed in Sec. 2.3.

2.2 Cosmology

The Hubble Constant, H_0, describes the current expansion rate of the universe, but recent measurement of the late and early universe yield conflicting values with a current discrepancy reaching 5σ. Local measurements (ie. "late-universe method") commonly use Cepheid variable stars to calibrate the distances to Type 1a supernovae yielding

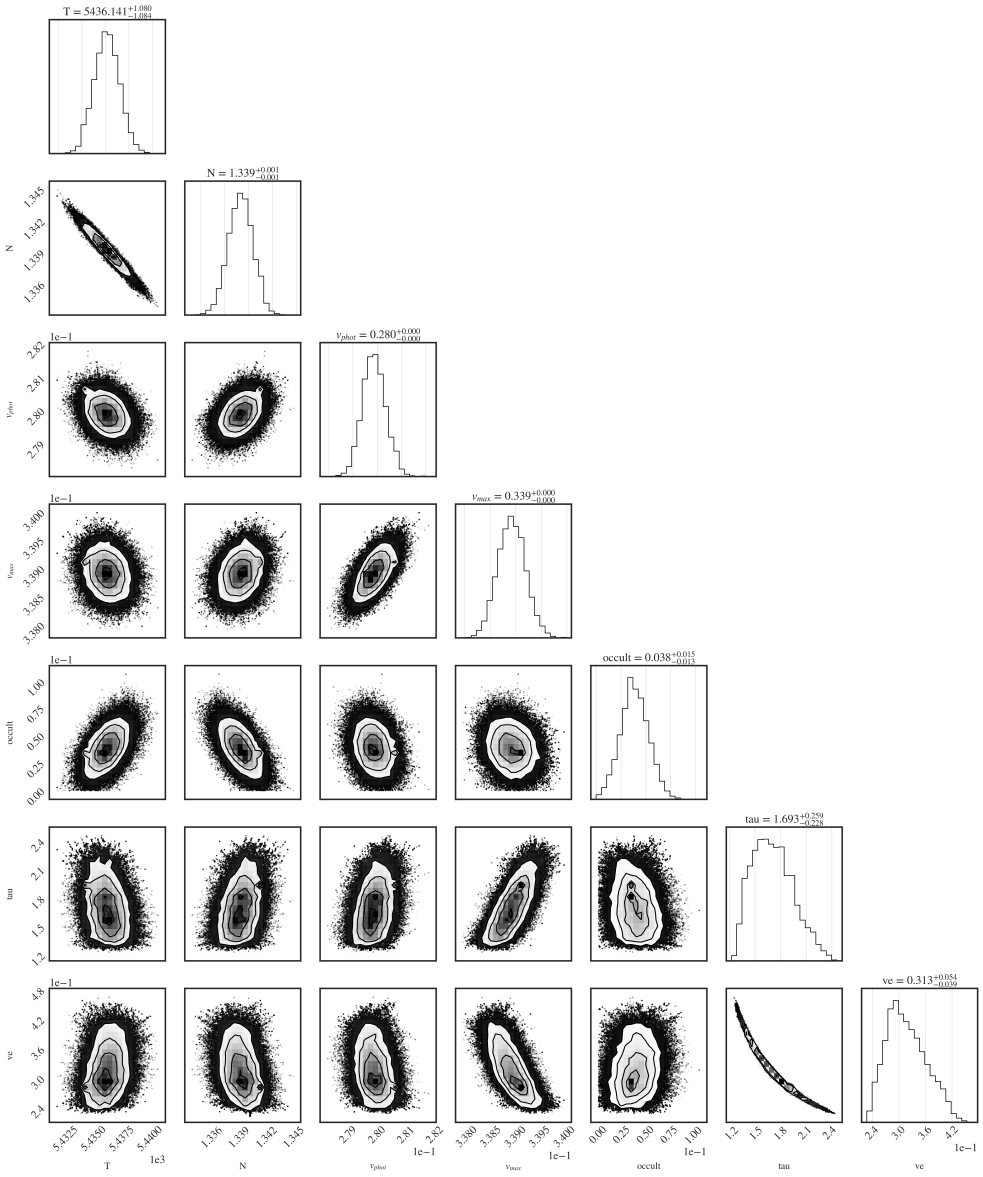

Figure 7: **Corner plot indicating posterior distribution of several key parameters for first epoch.** The posterior distribution is convex with singular global minimum. The parameters shown are 1) the blackbody temperature T, 2) the blackbody normalisation $N \cdot 10^{30}$, 3) the photospheric velocity v_{phot}, 4) the maximum ejecta velocity v_{max}, 5) the relative strength of the emission to absorption, 6) the optical depth of the line τ, and 7) the scaling velocity of the optical depth, v_e.

$H_0 = 73.03 \pm 1.04 \frac{km}{sMpc}$ [17]. In contrast, the early universe method, commonly fits the standard ΛCDM cosmology to temperature anomalies within the Cosmic Microwave Background (CMB), which yields an $H_0 = 67.36 \pm 0.54 \frac{km}{sMpc}$ [18]. Resolving this tension may require physics beyond the standard cosmological model of ΛCDM.

However, a suite of potential systematic errors could bias inferred values of H_0 for either measurement techniques. Thus, developing independent estimates are required. In this context both Gravitational Wave Standard Siren [10] and standardizing kilonovae [30] have been suggested as independent probes. For GW170817, the gravitational standard siren measurements yields an $H_0 = 70^{+12.0}_{-8.0} \frac{km}{sMpc}$ [10]. However, combining the siren with very long baseline interferometer of the centroid motion and afterglow lightcurve of the jet, can further constrain the degeneracy between the luminosity distance and observing angle. This yields a tighter constraint with $H_0 = 68.9^{+4.7}_{-4.6} \frac{km}{sMpc}$ [31]. Ultimately, the large statistical uncertainty make these methods currently consistent with both late and early universe measurements.

As shown in § 3, the expanding photosphere method provides consistent and tighter constraints on the luminosity distance to AT2017gfo and NGC4993 than any established methodologies including GW Standard Sirens [10, 31], surface-brightness fluctuations [56] and (examples, etc). Comparing the EPM estimated distance to kilonovae with the cosmological redshift of the host galaxy, we can now determine an independent constraints on the Hubble constant, H_0. For $z \ll 1$, Hubble's law gives the approximate luminosity distance (with $q_0 = -0.53$ for standard cosmological parameters):

$$D_L \approx H_0 c z_{cosmic} \left(1 + \frac{1 - q_0}{2} z_{cosmic}\right) \tag{8}$$

Here $z_{\rm cosmic}$ is the recession velocity due to the Hubble flow, i.e. correcting the observed redshift with respect to the CMB restframe, $z_{\rm CMB}$ for the peculiar velocity $z_{\rm pec}$. Absorption lines yield tight constraints on $z_{\rm CMB} = 0.01077 \pm 0.00018$. However, the host-galaxy NGC4993 is relatively near ($D_L \approx 40$ Mpc), so due to poor observational constraints on peculiar velocity, the cosmological redshift uncertainty is the dominant uncertainty in estimating H_0. Notably, there are a number of possible methods that

can be used when constraining the peculiar velocities [57, 58, 59, 60]. The most recent analysis, using a statistical reconstruction method which estimates large scale velocity flow using the Bayesian Origins Reconstruction from Galaxies (BORG), determines $z_{\rm pec} = 0.00124 \pm 0.00043$ [59]. This yields a cosmic recession velocity of $z_{cosmic} = 0.00952 \pm 0.00047$. Propagating these uncertainties into H_0 suggests that the EPM approach cannot statistically distinguish between early- and late-universe results with the single kilonova detection. However, with future detections especially at larger redshift this approach may yield precision constraint on H_0 (see Sec. 3.4). For future Kilonova-detection the uncertainty of peculiar velocity corrections will decrease, as more distant kilonova will be further within the Hubble flow. Additionally, the random direction of peculiar velocities will average out with more detections.

2.3 Line Asymmetry

In addition to the parameterization in § 2.1.2, which is intrinsically spherical, we have developed a P Cygni profile model from expanding atmospheres with an additional and free-to-vary eccentricity, e. This allows an independent probe of the sphericity by fitting the line shape. While in general constraints from the shape of spectral lines on the asymmetry of ejecta is degenerate with the viewing angle [61], in this case, good constraints on the inclination angle of the merger are provided by the radio jet emission with $\theta_{inc} = 21 \pm 7$ [48] and optical measurements $\theta_{inc} = 22 \pm 3$ [62]. Therefore, we can constrain the eccentricity of the ellipse by fitting the spectral line shape.

Physically, this parameterization is identical to the P Cygni profile in the Elementary Supernova, but assumes the photosphere has an elliptical shape. Thus, the contribution of the initial specific intensity and the source function is derived at each resonance plane integrated over the varying shapes of the expanding atmosphere. Note, this utilizes an identical functional dependence of the line optical depth with velocity, $\tau(v)$, for all angles, but varies effectively with angle because varying geometries and inclination angles yield different source functions, initial specific intensity and contribut-

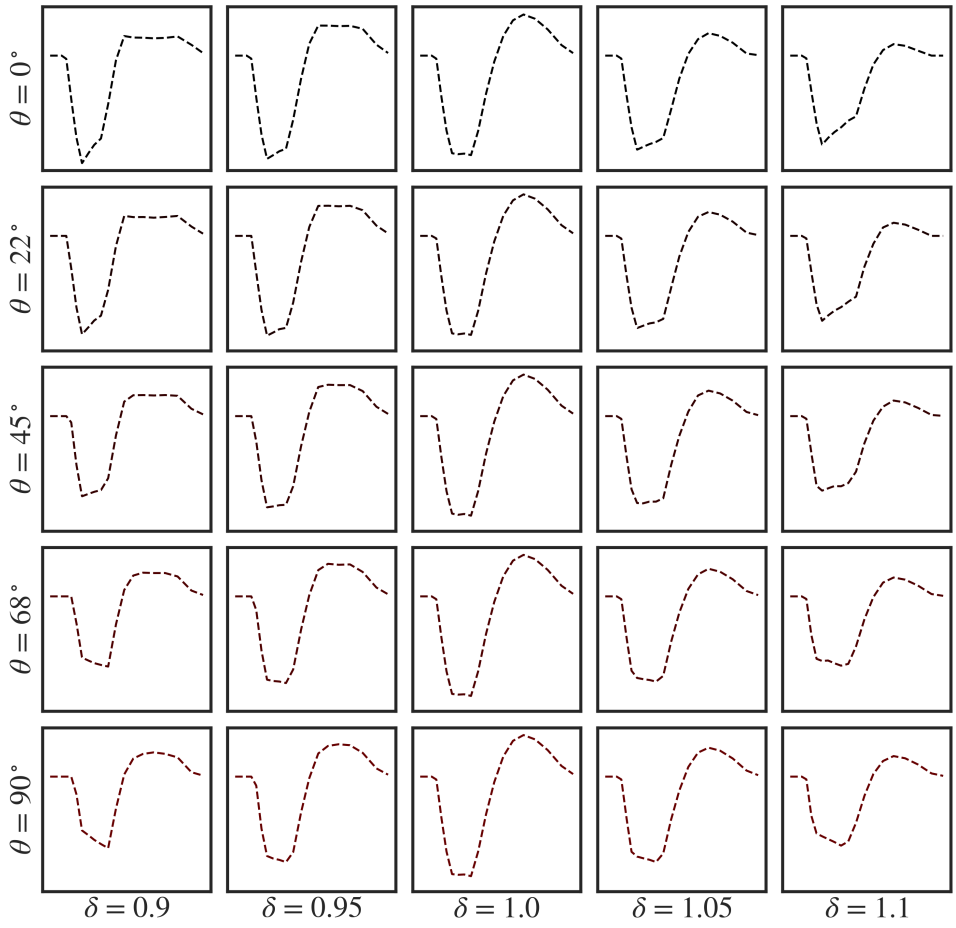

Figure 8: **Simulated P Cygni profiles with variable inclination, θ and ellipticity, δ.** Note for the fully spherical atmosphere (ie. $\delta = 1$) the absorption line is highly symmetrical. As δ increases, ie. with increasing oblateness, the transition from emission to absorption component becomes softer. Additionally, the inclination-angle sets the blue-to-red asymmetry of the absorption line.

ing resonance planes. Example P Cygni profiles for varying ellipticity and inclination angle are illustrated in Fig. 8.

2.3.1 Constraining a Simulated P Cygni Profile

In order to test our ability to constrain sphericity from line profiles, we have generated P Cygni with varying parameters and recuperated their properties within our uncertainties. This is exemplified in Fig. 9, where we illustrate the generated P Cygni profiles and the posterior parameter-landscape of the MCMC. For both the prolate and oblate geometry, we observe co-variances between the inclination angle, the photospheric velocity and the ellipticity of the expanding atmosphere. However, the overall shape remains well-constrained and our best-fit parameters matches the input parameters within the uncertainties of the posterior distribution.

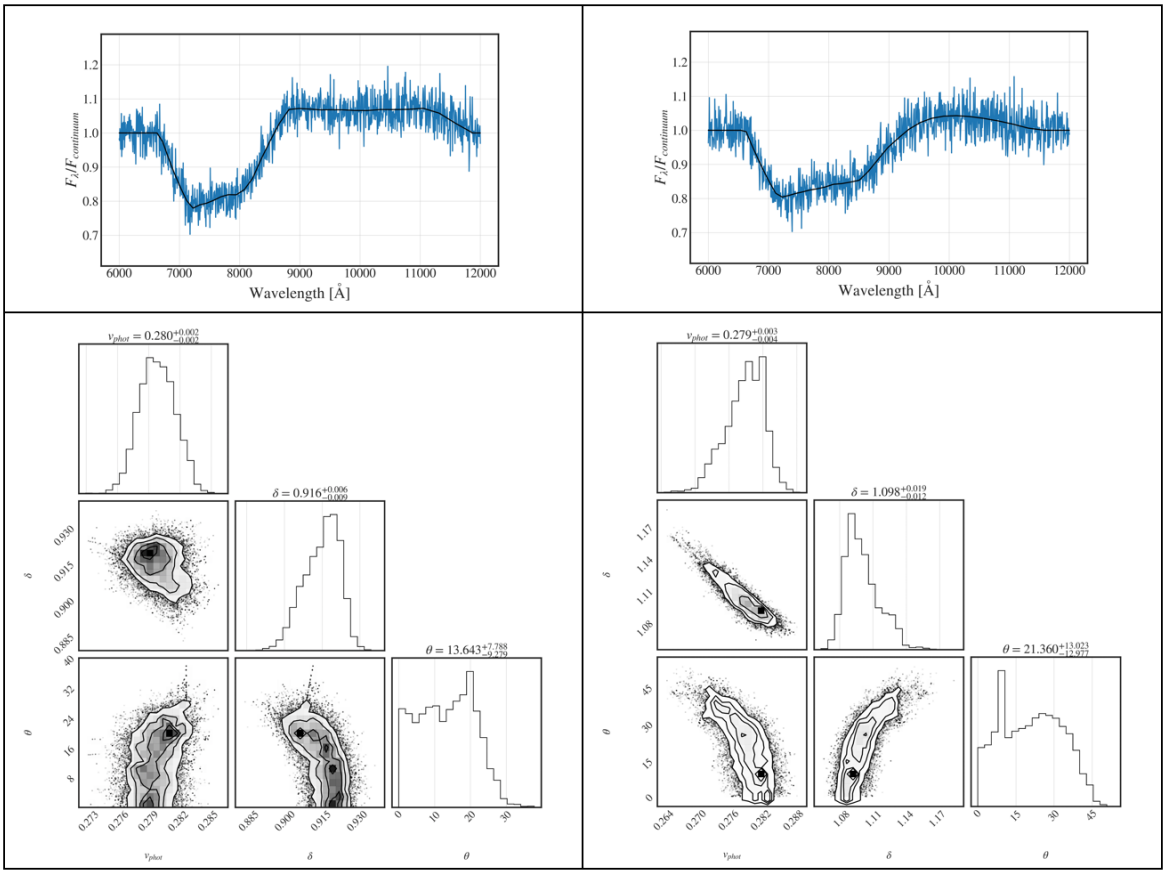

Figure 9: **Generated P Cygni profiles (top) with corresponding posterior sampled using MCMC (bottom)**. The simulated P Cygni profiles are generated assuming different ratios between semi-major and semi-minor axis with a prolate $\delta = 0.9$ (left panel) and oblate $\delta = 1.1$ (right panel). Note, the posterior distribution shows a complicated non-linear degeneracies between ellipticity and other parameters of the P Cygni (especially inclination-angle).

3 Results

The X-shooter spectrum and the final fit-models for each of the first five epochs are illustrated in Fig. 26. The overall continuum shape is characteristic of a cooling black-body while the absorption and emission around 810μm and 1000μm is well described by the P-cygni profile from the lines of Sr II (as previously confirmed in [16]). For later epochs additional spectral components of unknown origin emerge, which may potentially bias any estimation of the continuum flux. Despite the remarkable simplicity of the methodology, the analysis provides a suprisingly coherent and decent fit to the data.

We estimate R from the P-cygni profile and $T_{\rm eff}$ from the continuum shape for each epoch as seen in Fig. 11. For the epochs analysed $T_{\rm eff}$ is a monotonically decreasing function cooling from 5.400 K to 3.000 K. The radius of the photosphere monotonically increases, while its derivative (the photospheric velocity) is progressively decreasing as the photosphere recedes deeper within the ejecta. The sampling of the posterior distribution for later epoch can be found within Appendix.

3.1 Constraints on Distance

Given the EPM-framework (see Sec 2.1) we deduce the luminosity distances for each epoch independently as illustrated in the posterior distributions of Fig. 12. Firstly, we note the posterior distribution remains convex with a single global maximum for each epoch. Secondly, we observe only a small statistical scatter where each individual epoch is well constrained. The earliest two epochs remain consistent within 1σ despite tight statistical uncertainties. Assuming spherical symmetry the estimated luminosity distance for the first and second epochs are respectively $D_L(1^{\rm st}\ \text{epoch}) = 43.19 \pm 0.36$ Mpc and $D_L(2^{\rm nd}\ \text{epoch}) = 45.74 \pm 0.41$ Mpc. Notably, relaxing the requirement of perfect sphericity and instead propagating the uncertainty from the line-shape derived in Sec. 3.3.1 yields $D_L(1^{\rm st}\ \text{epoch}) = 43.69 \pm 0.85$ Mpc and $D_L(2^{\rm nd}\ \text{epoch}) = 45.70 \pm 0.91$ Mpc. Across these two epochs, we are looking at significantly different periods for the

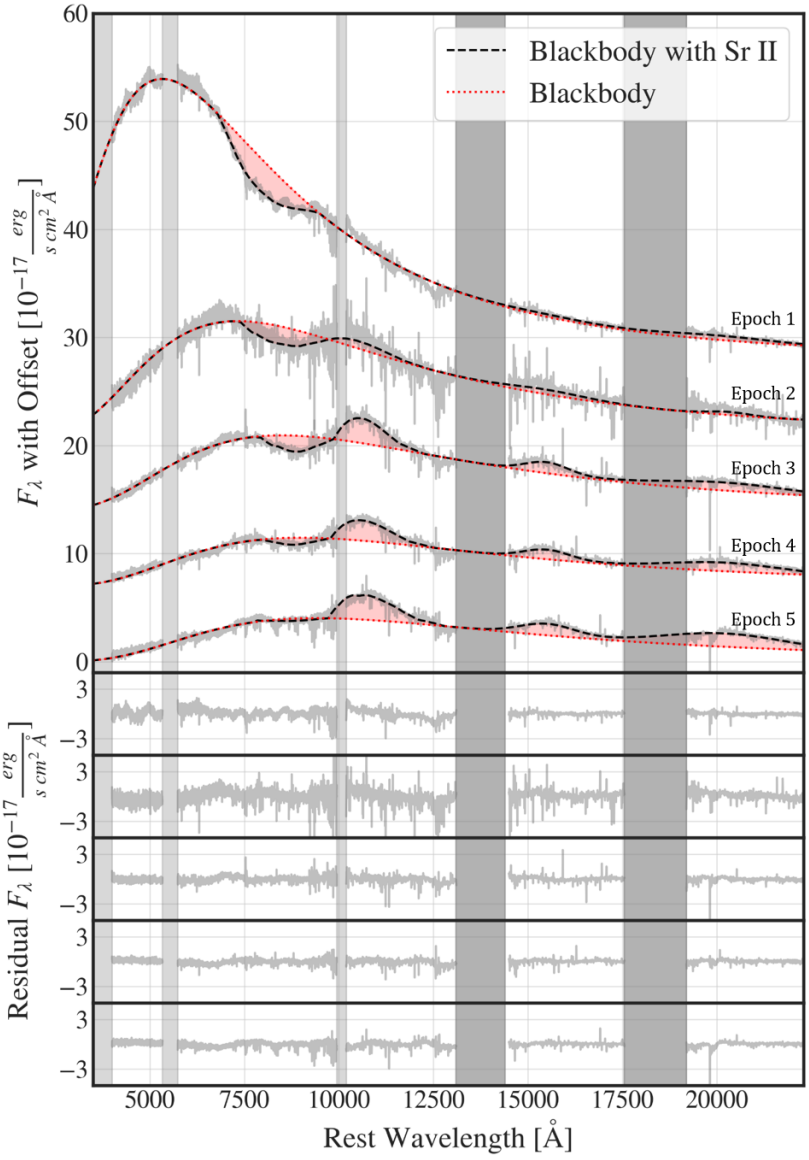

Figure 10: **Spectral series of AT2017gfo 1.4–5.4 days after the merger**. Spectra are from the VLT/X-shooter spectrograph (grey), with best fit shown with a dashed black line, and the blackbody-only component indicated with a red dotted line and deviations from the blackbody with pink fill. Grey-shaded regions were not included in the fits. Darker shaded bars indicate telluric regions; light grey indicates overlapping noisy regions between the UVB, VIS and NIR arms of the spectrograph.

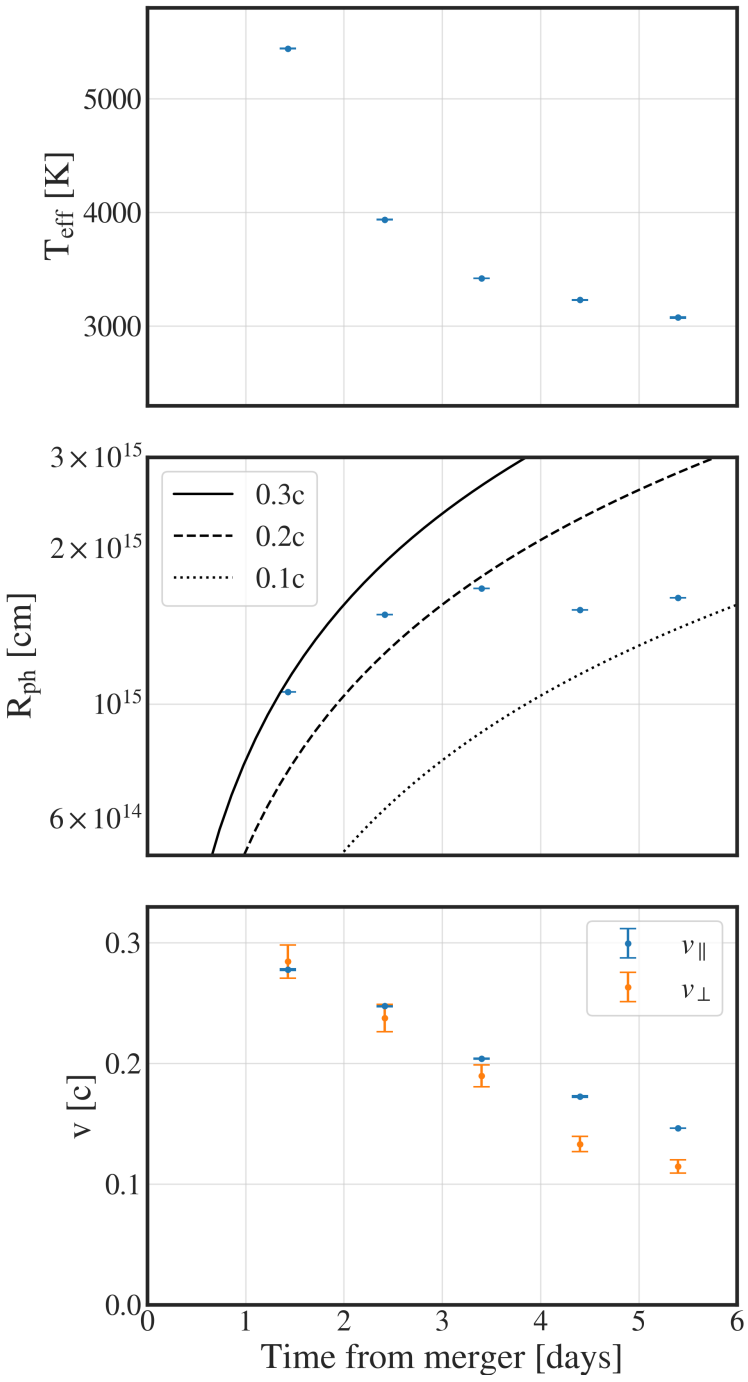

Figure 11: **Best-fit parameters from epochs 1-5**. Top panel contains the effective temperature, middle panel the radius of photosphere and the lower panel indicates the velocity constrains with the continuum constraints, $v_{\perp}$, and the photospheric velocity of the line, $v_{\parallel}$. The errorbars indicate the 16th and 84th percentiles as the uncertainty.

ejecta. There is almost a two-fold increase in time passed since the merger, but both the blackbody emitting area and the velocity of the line move coherently deeper within the ejecta producing a broadly consistent distance. Ultimately, despite the significant evolution of the ejecta and the surrounding atmosphere over these two epochs, the approach remains internally consistent and seemingly provides high-precision constraints on the distance to NGC4993.

While the inferred distance is seemingly tighter in its constraining power than prior analysis, it is consistent with all of the current distance estimates including the standard siren distance from the gravitational waves[31], surface brightness fluctuations [56], the fundamental plane [57], and the distance inferred from the cosmological redshift for either the CMB[18] or local distance-ladder[17] inferred H_0 value. We emphasise, that despite the significant evolution of the ejecta and the surrounding atmosphere over early two epochs, the overall results remain robustly within prior constraints and potentially provide an avenue for percentage precision on the distance to NGC4993.

3.2 Constraint on inclination angle

This distance is also useful because we can combine our distance measurement with the gravitational wave standard siren data[11] to infer the angle of inclination of the merger plane (Fig. 13). Here we utilize, the fact that the standard siren constraints on distance are highly covariant with the inclination-angle. Thus, by constraining the distance, we can improve the estimate of the spatial orientation of the merger. We find, assuming spherical symmetry of the kilonova, that the merger is inclined at 16^{+7}_{-6} from the axis perpendicular to the plane. This is consistent with the inclination inferred from very-long-baseline interferometry (VLBI) of the jet associated with the event, which is 21 ± 7 [48]. Naturally, it is also consistent with the combined constraints from VLBI and Hubble Space Telescope precision astrometry with 22 ± 3 [62]

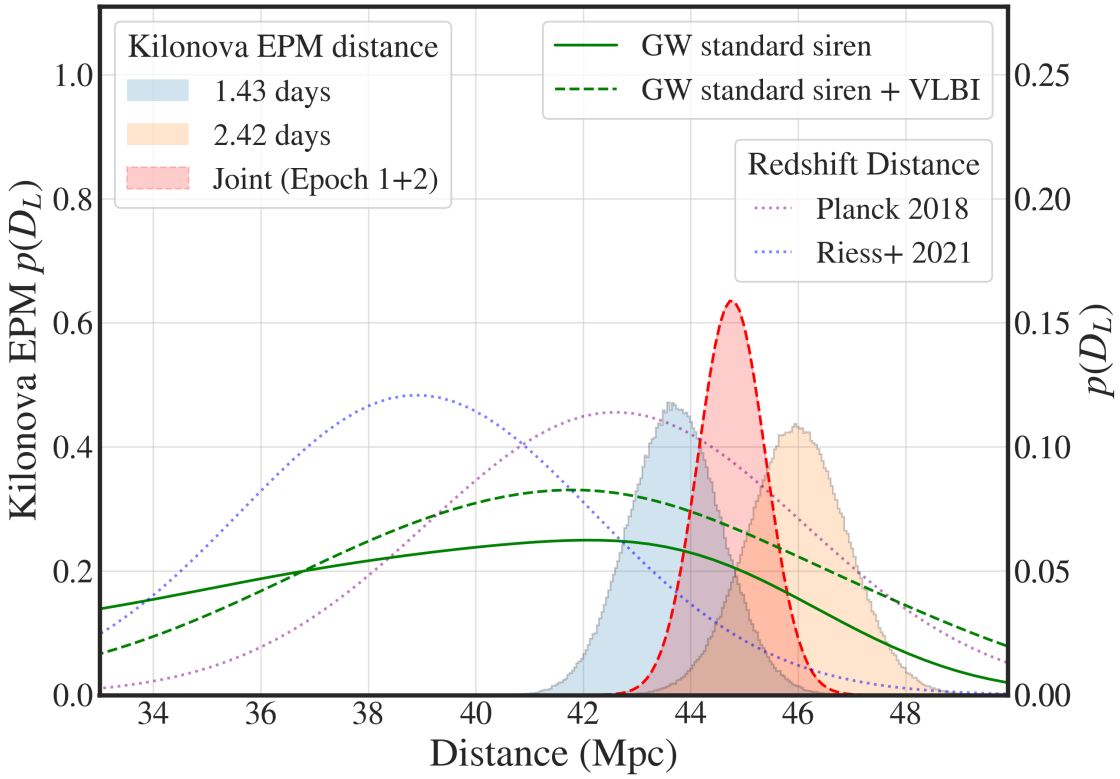

Figure 12: **Posterior probability distributions for the luminosity distance to the kilonova AT2017gfo.** Distance estimates based on the kilonova expanding photospheres method for the spectra obtained at 1.43, 2.42 days and the combined constraint from epochs 1+2 are shown as blue, salmon, green and red histograms respectively. Here, we do not assume spherical symmetry, but propagate the uncertainties from the line-shape constraint from Sec. 3.3.1. The gravitational wave standard siren distance estimate with and without very long baseline interferometry radio data are shown as dashed and solid green lines respectively. Cosmological redshift distances are also plotted, assuming $H_0 = 67.36 \pm 0.54$ [18] (dotted purple) and $H_0 = 73.03 \pm 1.04$ [17] (dotted blue).

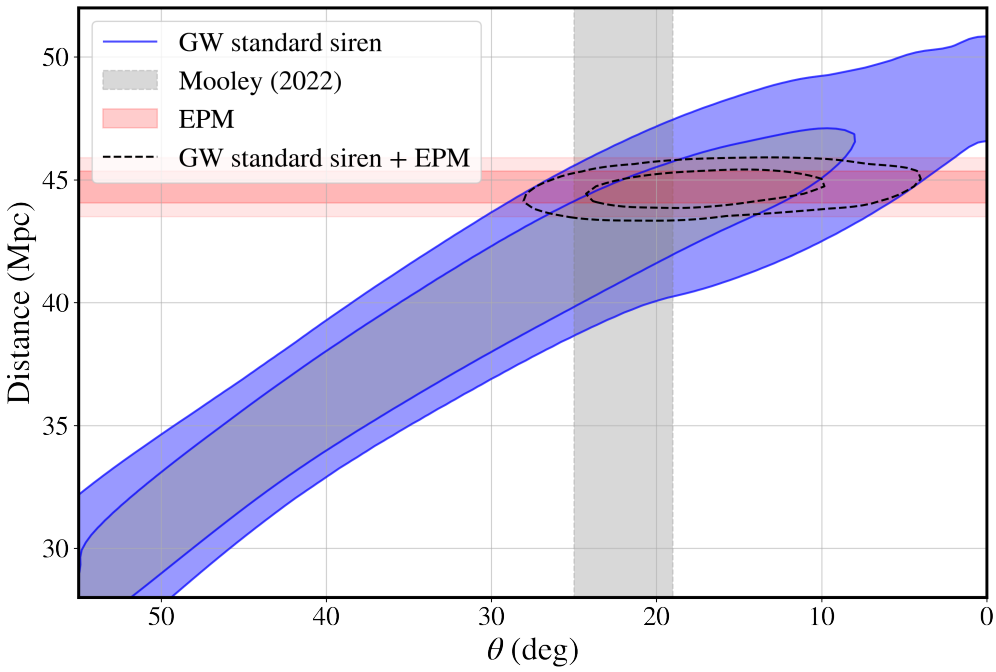

Figure 13: **Comparison of the inclination angle and luminosity distance to AT2017gfo compared to the inclination angle constraint from VLBI jet measurements.** The posterior probability distribution (dashed contours) from the combined EPM (red) and gravitational wave standard siren volumetric (blue) priors yield a tight constraint on the inclination angle, in close agreement with constraints from VLBI measurements and Hubble Space Telescope precision astrometry (grey shading [62])

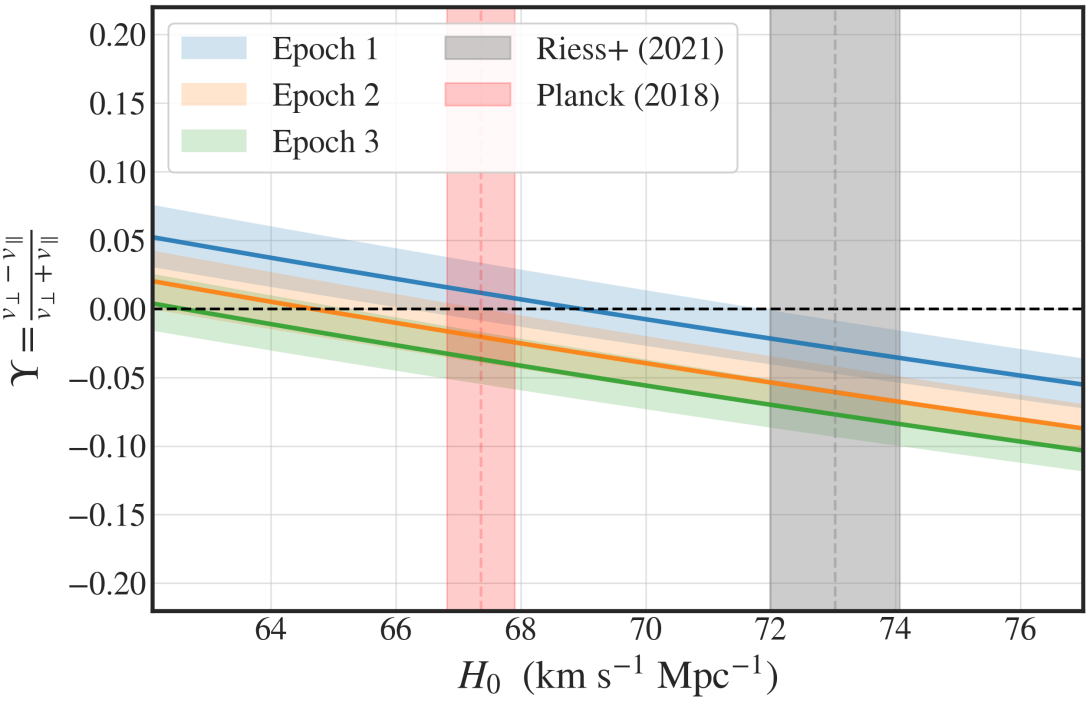

Figure 14: **Kilonova asymmetry index as a function of H_0.** The measurement of the asymmetry, Υ, and the Hubble constant are strongly degenerate, with higher H_0 implying more prolate ejecta. Both early-universe (i.e. CMB) and late-universe estimates of H_0 suggest that the kilonova is close to spherically symmetric, with less than 10% variation between the velocities.

.

3.3 Constraint on Sphericity

Assuming a cosmological distance of 44.2 ± 2.1 Mpc, based on a host galaxy peculiar velocity of 360 ± 140 km/s [59] and the cosmological model of ref [18] which has a Hubble constant $H_0 = 67.36 \pm 0.54$ derived from the cosmic microwave background (CMB), we can now determine our degree of asymmetry, $\Upsilon = \frac{v_\perp - v_\parallel}{v_\perp + v_\parallel}$. For the kilonova for epochs 1 and 2, we find $\Upsilon = 0.00 \pm 0.02$. The dominant uncertainty in Υ is the cosmologically-inferred distance to the source, whose uncertainty depends mostly on

the peculiar velocity of the host galaxy, NGC 4993.

For varying priors on H_0 one may determine slight variations in inferred distance and in extension in $v_\perp$ or Υ (as detailed in Fig. 14). Using instead the local distance ladder $H_0 = 73.03 \pm 1.04$ [17] yields an asymmetry $\Upsilon = -0.04 \pm 0.03$, which remains consistent with full spherical symmetry to a high degree of accuracy. Constraints on the kilonova's asymmetry from spectropolarimetry at 1.43 days are consistent with this spherical geometry, but are not very constraining by comparison [63, 64].

3.3.1 Constraint from Line Shape

As detailed in Sec. 2.3, we can also infer the sphericity of the ejecta in an entirely independent way by analysing the shape of the absorption line. We fit the P Cygni profile of an elliptical expanding atmosphere to the emission and absorption feature observed at 0.8–1.1 μm. These independent line shape sphericity constraints are shown in Fig. 15. For every epoch we find a line shape that is consistent with a completely spherical expansion to within a few percent. However, towards later epochs the line asymmetry grows and becomes increasingly prolate.

The line shape is sensitive to the angular distribution of Sr in the expanding atmosphere with the spherical expansion of Fig. 15 suggesting a near spherically symmetric distribution of Sr^+. This contrasts and complements the constraint on sphericity from the expanding photospheres method, which, while more robust and model independent, only constrains the total opacity, not the opacity in any given element.

3.4 Future Constraints on the Hubble Constant

If the sphericity constraints provided by the line shape (and somewhat corroborated by the consistency in the EMP-analysis) truly is indicative of the sphericity of AT2017gfo, the estimate of luminosity distance in Fig. 12 can be directly translated into a cosmological constraint on H_0. The Hubble constant determined from the kilonova EPM-distance is illustrated in Fig. 16 for each of the first two epochs. We find

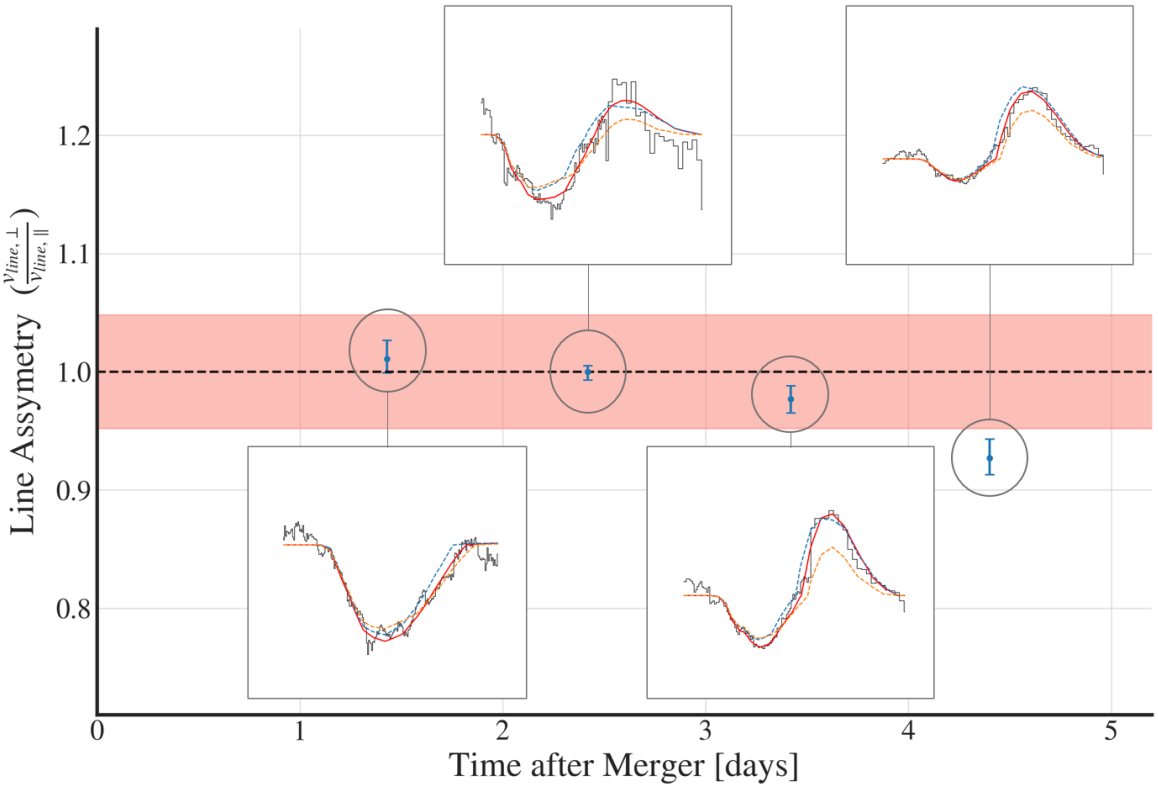

Figure 15: **Constraints on the spherical symmetry of the kilonova from the line shape.** For every epoch the expansion is consistent with spherical to within a few percent. The red shading indicates the sphericity constraints from the EPM method for epoch 1. Cutouts above and below the line show the residual to the blackbody fit around the 1 μm Sr II feature for each epoch. The P Cygni profile given fixed $v_{\parallel}$ is shown with varying ellipsoidal atmosphere shapes as follows: 5 % prolate (blue dashed line), spherical (red line), and 5% oblate (orange dashed line).

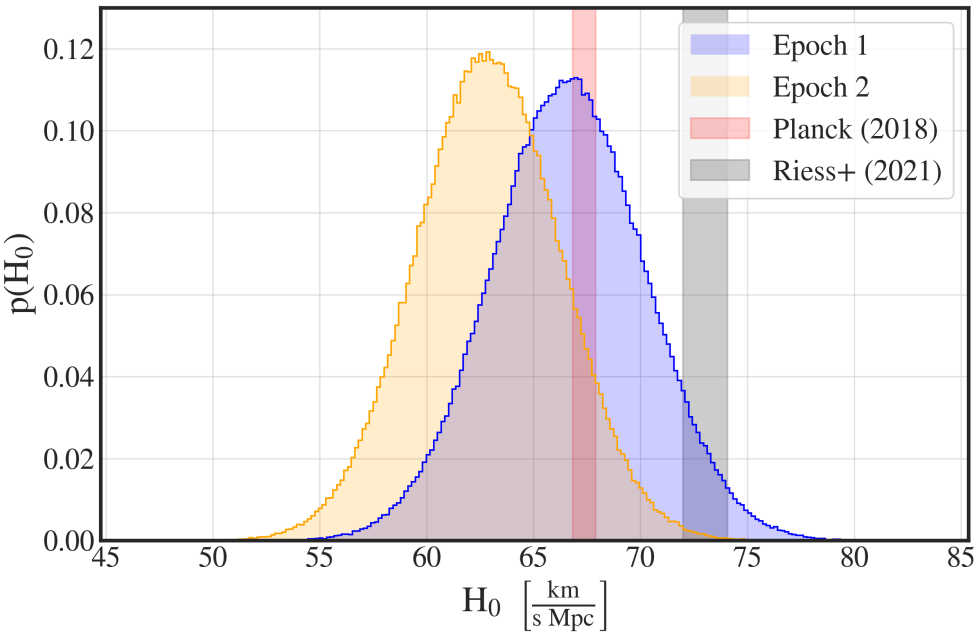

Figure 16: **Constraints on the Hubble Constant for distances derived from Epochs 1 and 2.** Due to the large peculiar velocity uncertainties, both epochs are broadly consistent with both late- and early-universe cosmological parameters.

$H_0 = 64.3 \pm 3.5\,\mathrm{km\,s^{-1}\,Mpc^{-1}}$ using the weighted distance from both epochs. The tight constraints on luminosity distances we find means that the peculiar velocity is our dominant uncertainty when estimating H_0. While this H_0 is closely aligned with the Planck cosmology [18], the large uncertainty does encompass the local distance ladder H_0-value within 3σ [17].

Ultimately, any analysis of the kilonova AT2017gfo cannot yield precision estimates on cosmology due to the large peculiar velocity uncertainties of NGC4993. However, with numerous additional kilonova observations with optical counterparts expected for the upcoming O4 and O5 runs using the Advanced LIGO, Virgo and KAGRA (HLVK) network, significantly tighter constraints are expected for a few key reasons [28]. Firstly, with larger sample size the statistical uncertainty will decrease, while the random direction of peculiar velocities will average out. Secondly, due to increased

GW-sensitivity future kilonova are expected at greater distances, where the fractional impact of peculiar velocity uncertainties are smaller. However, larger distances will also result in fainter optical counterparts with correspondingly smaller SNR. Thirdly, ongoing peculiar velocity surveys will improve the accuracy of peculiar velocity models [65]. In the following, we will provide an order of magnitude estimate on the potential constraints attainable with EPM subject to the assumption that AT2017gfo is representative of future detected kilonovae.

To quantity *the statistical distance uncertainty* the EPM-framework will yield for future detections at larger distances, we generate and fit mock-spectra at variable SNR. In Fig. 17 we indicate the fractional uncertainty on luminosity distance obtained from a single object with an identical intrinsic luminosity as the 1st epoch spectrum, but placed at greater distances (ie. by diluting the flux over the surface of a sphere with radius D_L). Thus, the mock object at 43 Mpc has identical SNR as the observed 1st epoch spectrum of AT2017gfo. Naturally, the statistical uncertainty of the fit increases monotonically, but only reaches a fractional uncertainty of $\approx 1\%$ for a detection at 150 Mpc.

Additionally, *the systematic distance uncertainties* associated with flux-calibration, dust extinction or the degree of asphericity contribute to the error budget. The relative contributions of each of these are set by the favorability of observing conditions, for instance the quality of coincident photometry for flux calibration, the reddening for the specific object for dust extinction or the constraining power of line-shapes or spectropolarimetry analysis for asphericity. For AT2017gfo the dominant systematic remains the constraints on sphericity of the ejecta, which is independent of distance. Thus, for future kilonovae detections at higher distance the fractional uncertainty from systematics are unchanged (see Fig. 17).

In contrast, to first approximation *the typical peculiar velocity uncertainty* is independent of distance, so the fractional uncertainty decreases as D_L^{-1}. Further, if the peculiar velocity uncertainty of NGC4993 is representative of future kilonova, we have an anchor on $\sigma_{z_{cosmic}}$. Subject to these two conjectures, the peculiar velocities remain

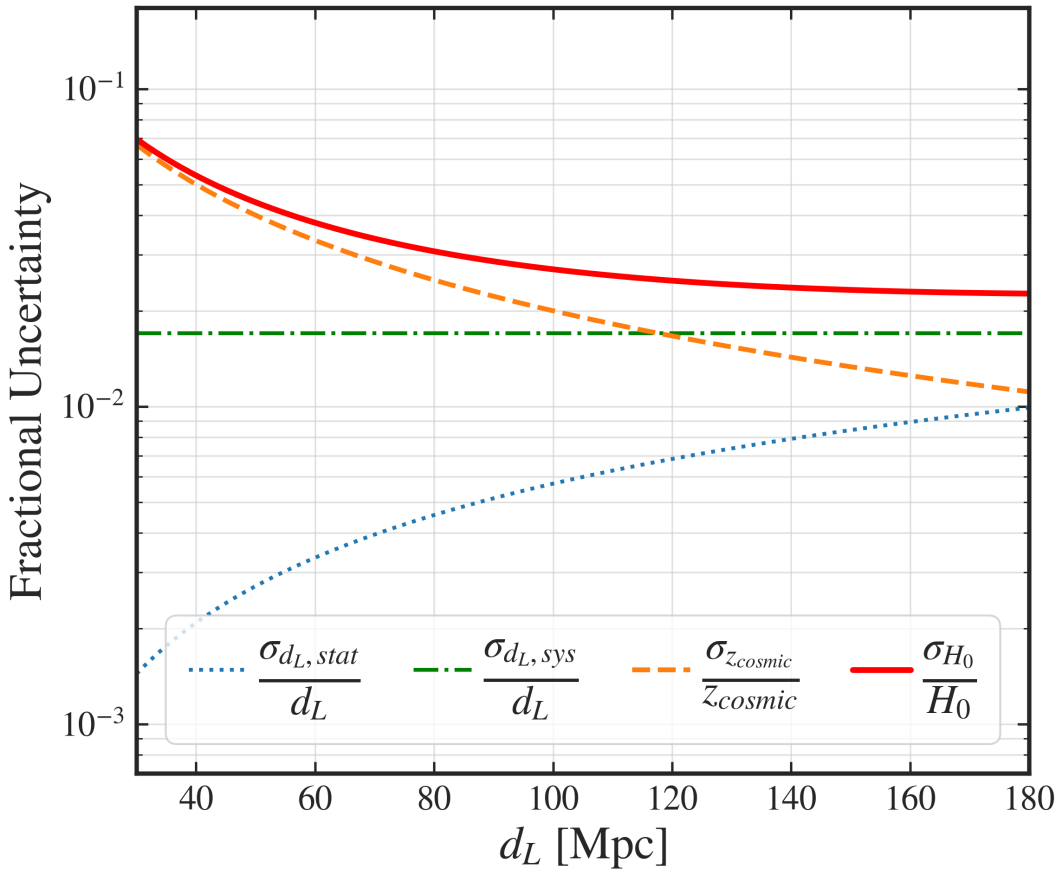

Figure 17: **Fractional uncertainty on H_0 (red line) for a future kilonova detection with similar intrinsic luminosity, systematic uncertainties and peculiar velocity uncertainty as AT2017gfo**. The dominant contribution for $D_L < 120$ Mpc is the fractional uncertainty from recession velocity (dashed orange line) assuming the total peculiar velocity uncertainty is independent of distance. The statistical uncertainty on luminosity distance for mock spectra objects with same intrinsic luminosity as 1st X-shooter epoch increases with distance (blue dotted lines). The systematic uncertainties in distance from sphericity-constraints, flux-calibration and dust-extinction are generically independent of distance.

BNS mergers	1	5	10
$\frac{\sigma_{H_0}}{H_0}$	2.5%	1.1%	0.8%

Table 1: Future number of kilonovae detected with GW and optical counterparts versus the expected fractional constraint attainable on H_0. All mergers are assumed to be uniformly distributed within the observable volume of the HLVK network during the O4-run, with identical intrinsic luminosity and peculiar velocity uncertainty as AT2017gfo.

the dominant uncertainty up to $D_L \approx 120$ Mpc, as illustrated in Fig. 17. An individual kilonova-observation at $D_L \approx 150$ Mpc with both GW-signatures and follow-up high-resolution spectra could yield 2.5% precision estimates of H_0.

The largest unknown in future constraint capabilities is estimating the number of binary neutron star (BNS) mergers. Current estimates suggest O4 detection sensitivity is up to $D_L \approx 150$ Mpc with around 10^{+52}_{-10} BNS detections per-calender-year [66]. Approximately 40% of these events are expected to have a 90% credible region smaller than 20deg^2. Thus, a significant fraction of GW-detections is expected to have optical counterparts. In Table 1, we therefore show the expected constraint on H_0 attainable with 1, 5 or 10 detections with similar intrinsic luminosity and peculiar velocity as AT2017gfo. These detections are assumed to be uniformly distributed within the observable volume of the HLVK network during the O4-run. Given a detection sensitivity up to 150 Mpc, this suggests the typical BNS merger will be at $D_L = 119^{+22}_{-36}$ Mpc. Ultimately, this provides preliminary evidence that applying EPM to kilonovae may yield precision cosmological constraint given a handful of early detections.

3.5 The emergent line; the 0.75μm P Cygni

The entire analysis of this thesis has centered on the complementary constraint from the Sr^+ lines and the continuum flux. While these are the dominant features and provides adequate description of early spectra, there are a series of emergent features at late times (as mentioned in Sec. 2.1.3). The spectral origin of these absorption, emission and P Cygni profiles remain as of yet unknown. Nevertheless, the wealth of spectral information hidden within these lines may provide further complementary or contrasting probes of the kilonova structure.

Therefore, we have also searched the spectra and our residuals for novel line detections and the constraints they may allow. Of these the most promising candidate, is an emission line at $\approx 0.75\mu$m with a seemingly associated absorption line at $\approx 0.65\mu$m visible from the 4th epoch and onwards. These features can be seen in Fig. 18, where their combination produces a remarkable clean P Cygni profile. By assuming this featured is produced (or at least can be approximated) by a singular line, we can fit the P Cygni structure using the prescription discussed in Sec. 2.1.2. The central wavelength of the line is well-constrained from the emission feature and fitting it from the 4th epoch (the epoch with highest signal to noise) yields $\lambda = 0.7505 \pm 0.0008\mu$m. While the statistical uncertainty remains very tight, we emphasise that there are significant unknown systematics, which can bias the central value. Firstly, with no prior spectral identification, we assume the origin of the line to be from a single transition when a blending of nearby lines may produce a similar profile. The spectral evolution over all epochs 1-10 is generally characterised by an increasing number of emergent lines, which may make the single line fit progressively more tentative. Secondly, any potential fluorescence of the line may bias the overall shape [67]. Thirdly, the relativistic velocity of the ejecta moving at $\approx 0.15c$, suggest that there are significant time-delays which imply the different wavelengths of the profile may be probing different times, ie. at different temperatures and optical depths.

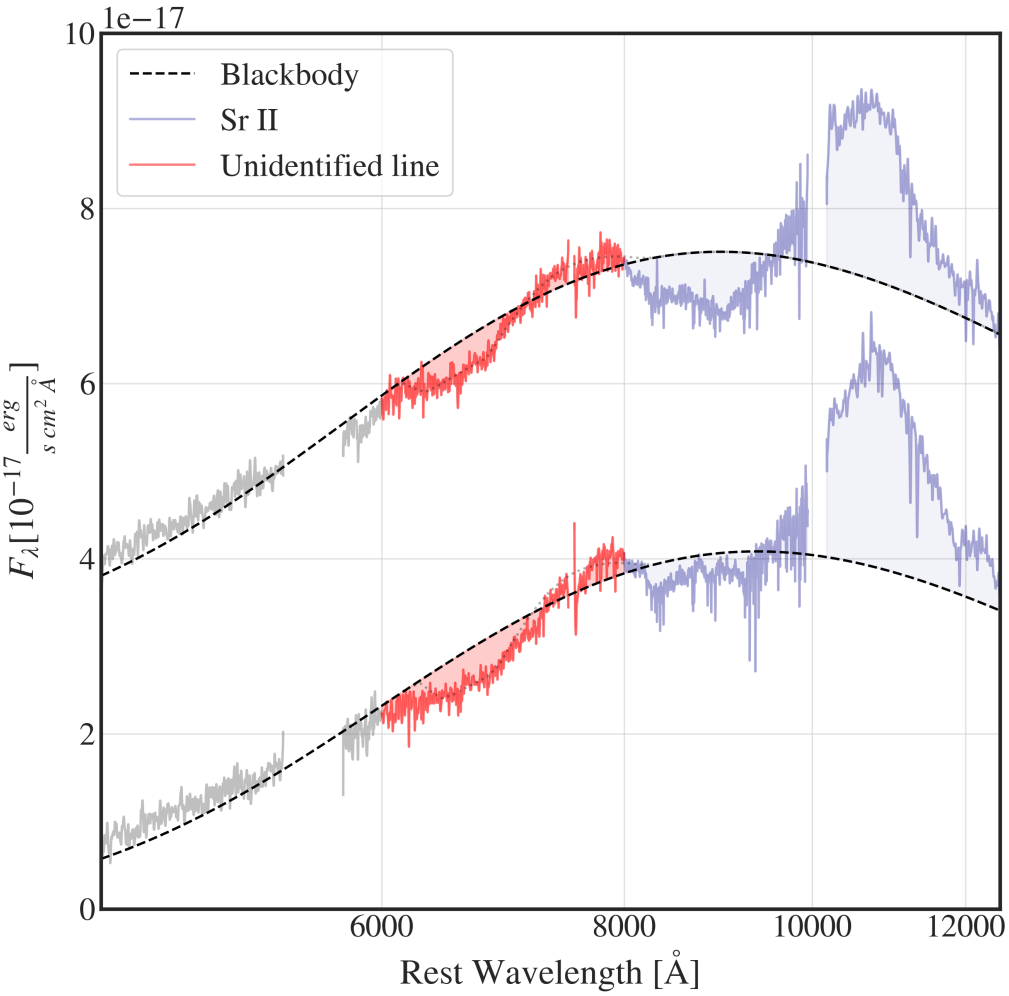

Figure 18: **X-shooter spectrum for epochs 4 and 5**, which emphasises features in the wavelength-range from 4.000 Å to 12.500 Å. Notable the two largest features, the unidentified 0.75μm and Sr^+ P Cygni, share a similar spread in wavelengths.

Determining its spectral origin is a matter of ongoing research, but any search is inherently limited by the current incomplete line-lists of r-process elements. We have examined the line lists of the most obvious spectral candidates, ie. with strong transitions due to a small number of valence electrons and low-lying energy levels [68]. Firstly, the elements near the first r-process peak, which are abundant and contain the only known prior identification, Sr. Of these elements neither Ru, Sr or Zr have any strong lines at the relevant wavelengths for their likely ionization potentials. Y II has a strong line transition at 0.788μm, but this remains significantly above the statistical uncertainty of the fit, which would require a large bias of the systematics. While there are several remarkable congruent and strong lines from second r-process peak elements (notable Ba I, La I), physical conditions allowing these lines should typically have a series of lines from nearby isotopes or elements, which are not evident for the AT2017gfo spectra. Ultimately, no identification from the limited current line-lists are entirely satisfactory.

Furthermore, the velocity stratification of the line provides an independent estimate of the velocity-structure of the ejecta. The velocities derived are generically more uncertain as the optical depth of the line is small, the line identification remains unknown and the later epochs have more less accurate constraints on the continuum flux. Given all these caveats it is remarkable that the overall spread in wavelength is similar for both the novel line and the Sr^+ lines. Fitting both P Cygni suggests the ejecta has a photospheric velocity of $\approx 0.18c$ and $\approx 0.15c$ for both lines for epoch 4 and 5 respectively. Curiously, neither line in these later epochs are in agreement with the cross-sectional velocity, $v_\perp$, inferred by the blackbody continuum as shown in Fig. 19. While this is potentially caused by the large systematics uncertainties and difficulties associated with constraining the continuum in later epochs, if this feature is persistent, this may hint at an increasingly prolate ejecta in later epochs. Indeed, the increase of $v_\parallel$ relative to $v_\perp$ in later epochs is already indicated from the line-shape constraints

illustrated in Fig. 15.

3.6 The Multi-temperature Blackbody

The entire analysis presented, up to this point has assumed a singular blackbody continuum. However, it is worth emphasising that there are two dominant reasons why even an expanding photosphere with an intrinsic temperature, may not be well-described by an observed blackbody with a singular temperature.

Firstly, the projected velocity along the line-of-sight varies across surface-element, so the Doppler correction, and in extension the effective temperature, varies with the angle, θ, between the line of sight and the direction of expansion, ie. $T_{\rm eff}(\theta) = T_{\rm emi}\delta(\theta)$

Secondly, the light travel-time across the ejecta is on the order of days, in which time the ejecta itself cools rapidly. Therefore, the front of the ejecta (which is observed at the latest time of the expansion) is cooler than more distant portions of the eject. The cooling rate is constrained from follow-up photometry from best-fit blackbody models, that suggest effective temperatures from 0.5 to 5.5 days being consistent with a power-law decline in time $T_{\rm eff} \propto t^{-0.54\pm0.01}$ [49]. Note, this inferred rapid cooling observed in effective temperature is due to both the intrinsic cooling of rest-frame temperature and the bias of decreasing expansion velocities which lead to progressively less blueshifted ejecta. The photospheric approach [49] is further biased as it precludes any contribution of emission and absorption lines. For these reasons, the X-shooter spectrum and this complementary analysis provide the as-of-yet most comprehensive estimate of the evolution of blackbody temperatures for AT2017gfo. Fitting across epochs from 1.4 to 5.4 days after the merger, suggests a less-steep powerlaw with the rest-frame temperature decline being roughly consistent with $T_{emi} \propto t^{-0.46\pm0.05}$. Note, the powerlaw description of cooling is merely an approximation without a stringent theoretical foundation. Indeed, as the temperatures asymptotically approach $T \approx$ 3000K for later epochs, another functional prescription is clearly required.

Given the cooling powerlaw index, $T_{\rm power}$ and the velocity of the blackbody, v_{bb}, we

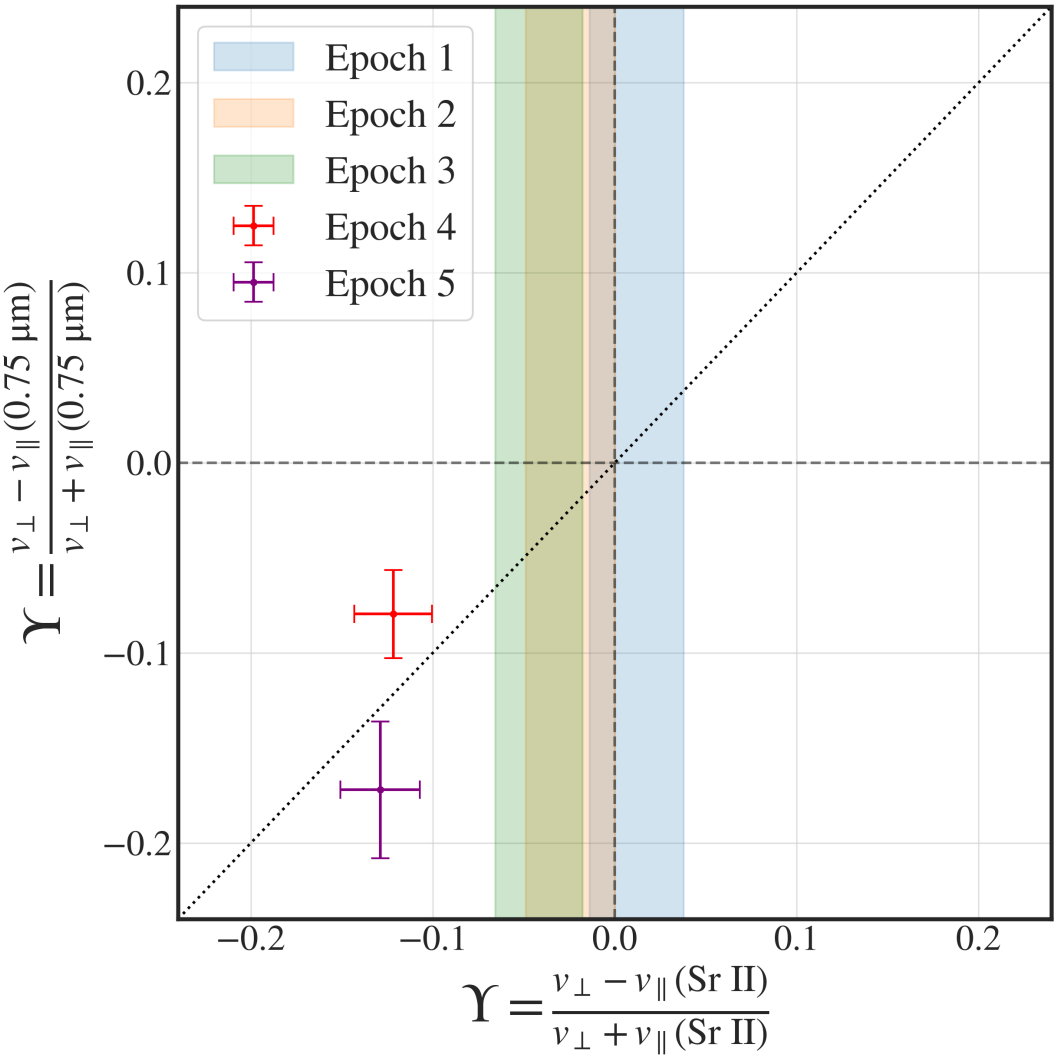

Figure 19: **Asymmetry constraints from Sr II and 0.75 μm P Cygni lines for AT2017gfo.** Asymmetry index assuming Planck cosmology comparing $v_\perp$ with $v_\parallel$ derived from Sr^+ and 0.75 μm line. Colored shading indicates constraints from epochs 1-3. While the lines broadly internally consistent, neither agrees with the cross-sectional velocity, which suggest an increasingly aspherical expansion at later epochs.

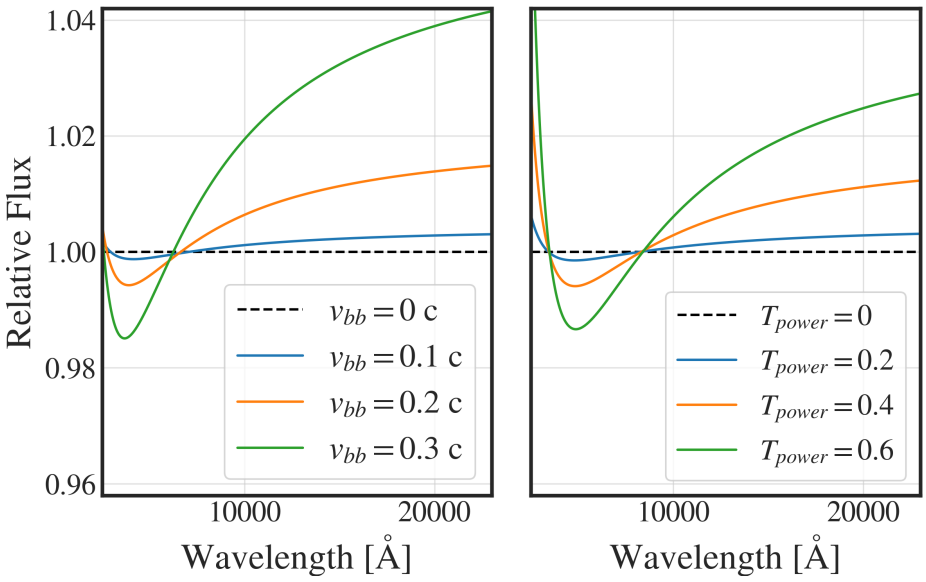

Figure 20: **The flux from convolving over the full photospheric surface relative to shifting by the average correction as a function of wavelength for a reference blackbody of 5000 K**. Left: the impact of velocity stratification in the Doppler correction for variable blackbody velocities. Right: the impact of temperature-cooling given variable cooling-rates, characterised by powerlaw-index T_{power}. Convolving over a range of temperatures or Doppler corrections lead to wider blackbody with a correspondingly less prominent peak.

can compute for each photospheric surface element the effective blackbody temperature:

$$T_{\rm eff}(\theta) = T_{ref} \left(\frac{t(\theta) - t_0}{t_0} \right)^{-T_{\rm power}} \delta(\theta) \tag{9}$$

Here, T_{ref} is a freely fitted reference temperature of the blackbody, t_0 is the time of initial explosion and $t(\theta)$ is the time when the observed photons were emitted from the surface element θ (ie. to parameterise the additional travel-time with larger θ). To determine the corresponding spectral shape, we must integrate the blackbodies over

the solid angle (and in extension over the range of effective temperatures):

$$F_\lambda = \int BB_\lambda(T_{\rm eff}(\theta))cos(\theta)d\Omega \tag{10}$$

Thus in conjunction the Doppler-correction and cooling rate set the range of effective temperatures of the photospheric surface, which in turn set the observed width of the blackbody spectrum. In Fig. 20, we illustrate the resulting change in blackbody shape caused by varying the line-of-sight velocities or temperatures of the photospheric surface. We note that to detect varying Doppler corrections from the spectral shape necessitates mildly relativistic velocities. Additionally, the spectral shape is only sensitive to the spread of effective temperatures, so there is a large degeneracy between varying rates of cooling and varying the Doppler correction. Nevertheless, in theory, for an observed spectrum containing well-constrained spectral lines the blackbody-width is fittable, which could empirically constrain the range of effective temperatures observed in a single epoch.

Indeed, the first epoch spectrum is well-constrained, with a distinct blackbody peak separate in wavelength from the P Cygni spectral component. Thus, this spectrum provides the clearest observational constraints on the blackbody width. While the cooling rate is highly degenerate with the blackbody velocity of expansion, the velocity of expansion is exceedingly well-constrained for any assumed cooling rate as seen in Fig. 21. Moreover, given the cooling rate derived from fitting across epochs ($T_{\rm eff} \propto t^{-0.46\pm0.05}$), the best-fit velocity stratification of the blackbody is $v_{bb} = 0.285 \pm 0.034$, which remains consistent with the photospheric velocity of the line, v_{phot}, and the velocity inferred from the total luminosity, $v_\perp$. We note for later epochs the width of the blackbody is ill-constrained, as the P Cygni spectral component begins overlapping in wavelength, a multitude of potential absorption and emission components emerge and the typical velocities (or equivalently Doppler-corrections) are smaller. However, this convolved blackbody framework may provide useful constraints for early observations of future kilonovae.

Notable, the three estimators of velocities involve different theoretical assumptions;

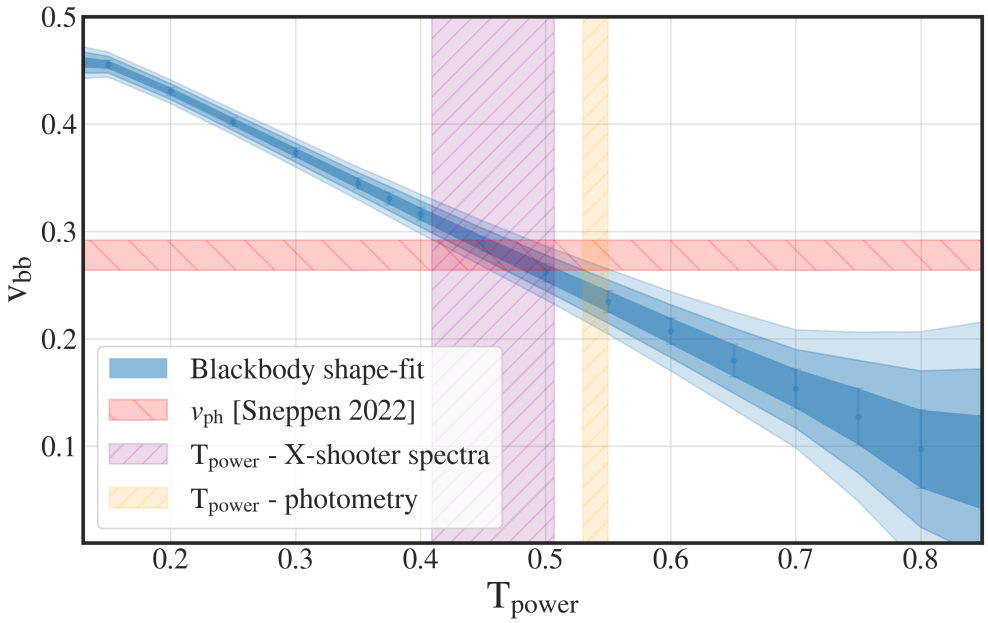

Figure 21: **Constraints on the expansion velocity v_{bb} given varying rates powerlaw cooling rates with powerlaw-index $T_{\rm power}$.** The red dashed region indicates the velocity, $v_\perp$, from the blackbody luminosity, which is in agreement with the velocity of the Sr^+ line. The purple and yellow region indicate cooling rates derived from fitting the effective temperature across epochs with spectra [13] or photometry [49]. Remarkably, the expansion velocity derived assuming standard cooling rates is in agreement with the other constraints on velocity.

The first, v_{bb}, requires constraints on the rate of cooling, the second, v_{phot}, on the spherical symmetry of the ejecta and the third $v_\perp$ requires an priori cosmology. Furthermore, these estimators are derived from different parts of the spectra, ie. the blackbody shape, the P Cygni lines and the overall normalisation. However, regardless of the varying theoretical assumptions and their statistical independence, all three estimators remain consistent for the first epoch. Conversely, any assumptions on cooling-rates, asymmetry or cosmology could now be tested against the other estimators.

4 Discussion

While the EPM application to Kilonovae has now seemingly provided sub-percent precision cosmological distances, an unexpected high-measure of sphericity and a framework for cosmological constraints of H_0, it does so by invoking a series of assumptions worth explicitly discussing. In the following we will deliberate on these potential suppositions, including the impact of time-delays, dilution factors, flux calibration, line blending and detached lines, to gauge their potential importance. Finally, we will summarize, why Kilonovae provide so apt physical terrain for the methods of expanding photospheres.

4.1 Limitations of EPM

4.1.1 Time Delay

Due to the high velocities of the photosphere, the ejecta quickly encompasses a large volume and the light-crossing time is considerable. This bias breaks spherical symmetry, with the blueshifted part of the photosphere being observed first (ie. later in the expansion history) and thus having had more time to expand than the more distant parts of the photosphere. A shock expanding with constant speed would due to time-delays appear as an ellipsoid elongated along the line of sight. Given the plane-parallel approximation [ie. $D_L >> r_{phot}$)], the apparent radius of the photosphere as a function of angle can be computed [69]:

$$r(t, \theta) = \frac{\beta(t - t_e)}{1 - \beta cos(\theta)} \tag{11}$$

Note, the semi-major axis (ie. the cross-sectional radius) is independent of time-delays. Therefore, the observed cross-sectional area is not affected by the time-delays of photons.

However, the ejecta velocity and temperature is evolving dynamically. In conjunction with the range of time-delays across surface-elements, this again indicates a singular blackbody may be overly simplistic for two reasons. First, the continuing cooling of the ejecta suggests the nearer front will have cooled further than the more distant,

earlier and hotter components of the photosphere. Secondly, the expansion is decelerating, which would result in a gradient in blueshifts (ie. larger relativistic Doppler corrections for distant portions of the ejecta). Both of these effects would theoretically contradict the assumption of a singular blackbody temperature, instead requiring convolving blackbodies over a continuum of temperatures as discussed in Sec. 3.6. Note, this convolution does require assumptions on the velocity- and temperature-profiles across epochs, which limits the statistical independence of the epochs. However, the singular blackbody provides a decent fit to the continuum across epochs and early epochs remain consistent despite varying rates of cooling which may indicate the small impact of time-delays.

Nevertheless, future radiative transfer codes should include and constrain the impact of variable travel-times on observed spectral energy distributions. It is worth emphasising that the corrections of time-delay are not conventionally applied to EPM analysis of SNe; However, SNe ejecta do have lower characteristic velocities with $v \approx 0.03c$, so the approximation may be more appropriate.

4.1.2 Flux Calibration

It is common practice to calibrate observed spectra to photometry by scaling the former to be consistent with the latter. However, the coincident photometric observations of AT2017gfo is not consistent across different instruments and publications. Therefore, any act of scaling the spectrum remains sensitive to an artificial choice of picking photometry as a calibration set. Nevertheless, the X-shooter spectrum of AT2017gfo remains broadly consistent with GROND, DECam, EFOSC2, LDSS, Swope and VIRCAM photometry across epochs, as illustrated for Epoch 1 in Fig. 22. Therefore we follow the convention in [16] and do not artificially scale the observed kilonova-spectra. However, we do inflate our errors on the normalisation to reflect the standard error in flux calibration of different instruments - thus ensuring our errors are robust regardless of choices for flux calibrating.

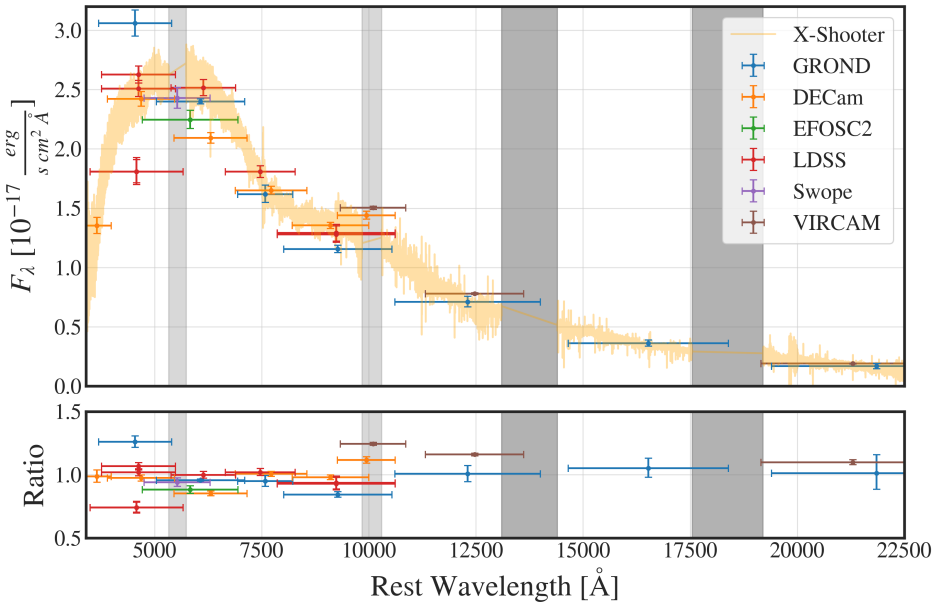

Figure 22: **X-shooter spectrum and inferred fluxes from photometry bands for the kilonova AT2017gfo across ultraviolet, optical and near-infrared for observations from 1.35 to 1.45 days after neutron star merger GW170817**. Dark shaded bars indicate telluric regions; Light shaded bars indicate overlapping noisy regions between the UVB, VIS and NIR arms. The ratio between spectrum and photometry (illustrated in lower panel) suggest the spectra are consistent with the weighted-average of photometric flux to within 1%

4.1.3 Dilution Factors

Historically EPM-analysis of SNe are limited to photometry which often requires correcting the luminosity from specific photometric bands by multiplying a factor ξ^2. Here ξ was originally introduced because the large contribution of electron-scattering opacity to the total opacity within the photospheres of SNe envelopes increases the photospheric radius (ie. the radius probed with Sr II) relative to the thermalisation radius (ie. the radius from blackbody continuum) [70]. However, in practice dilution factors also account for any deviation from the blackbody including the presence of lines

[71]. In contrast, within this analysis absorption and emission features of the spectrum are explicitly fit. The dilution factor for SNe are typically in the range $0.4 < \xi < 1.5$ with systematic discrepancies between different groups [72, 73, 74]. Importantly, these systematic discrepancies between competing models constitute one of the most significant sources of uncertainty in the EPM analysis of photometry and make any inferred distances essentially model-dependent. However, across models the correction-factors must decrease drastically with temperatures to ensure consistent distance measurements [71].

In contrast, while the color-temperature decreases significantly throughout the analysed epochs of the kilonova, the inferred luminosity distances remain broadly consistent without requiring correction-factors. This is because in kilonovae ejecta the electron scattering opacity is negligible compared to the opacity of bound-bound transition. The ratio is decreased for two reasons. Firstly, the opacity of bound-bound transitions is increased by several orders of magnitude due to the multiplicity of lines of r-process elements and the complexity of valence electron structure of elements within the r-process composition [75]. Secondly, the kilonova ejecta is composed of lowly ionized heavy elements, so the number of free electrons per unit mass is $\approx 10^{-2}$ smaller than the typical value for ionized hydrogen, and much less than the r-process line opacity at all wavelengths of interest. Thus, for the analysis of kilonovae one can assume the photospheric radius derived from the line is indeed at the thermalisation depth of the blackbody and no correction-factors for electron opacity are required to determine the distance.

Furthermore, it is worth emphasising that SNe photosphere are typically surrounded by a thick atmosphere, because of the late detection result in a photosphere residing deep within the ejecta [76]. In contrast, the unprecedented early spectroscopic follow-up of GW170817 allows an examination the blackbody spectrum during the buildup of the scattering atmosphere. Ultimately, a detailed modelling of radiative transfer, similar to the spectral expanding atmospheres method, may be required when examining later phases, but for the early epochs analysed in this thesis a pure blackbody with

emission features from the line-forming region and without dilution remains entirely self-consistent.

4.1.4 Line-blending

To address whether systematics, especially whether blending with other lines, could coherently bias the inferred line, we have tested the robustness of the derived velocities under a range of assumptions.

While the prior line identification of the 1 μm P Cygni as being due to Sr^+ [16] does provide a tight prior on the central wavelengths, this assumption is not central to our main conclusions. Indeed modelling a single emission, allowing the rest emission wavelength to be a free parameter, yields $\Upsilon = 0.03 \pm 0.02$ (assuming Planck cosmology), ie. still supporting spherical expansion. The result of spherical symmetry only requires that the observed P Cygni profile is indeed formed by a singular line or a series of close lines.

Adding to this complexity in modelling the profile is the potential effect of blending lines. This is problematic, as physically the unconstrained realm of kilonova composition yields little prior constraints on which potential lines may be present (and any spectral feature will be widely broadened due to relativistic velocities of the ejecta). Therefore, we explored the potential degeneracy of another line blending with the inferred P Cygni. We add an unidentified line to the fitting code, with a free-to-vary optical depth and rest wavelength (but similar velocity stratification as the Sr^+ lines). With a free additional parameters the goodness-of-fit prefers adding it near the central wavelengths of Sr^+ lines. While the strengths of these lines are now degenerate, as their rest-wavelength are similar, the photospheric velocity remains similar.

In Fig. 23 we show the inferred asymmetry index from the full-model with an additional P Cygni profile with varying central wavelength. The largest observed shift in Υ is 0.03, which happens when the new line is dominant and located immediately blue of the original Sr^+ lines. For no wavelengths do we shift the photospheric velocity to the

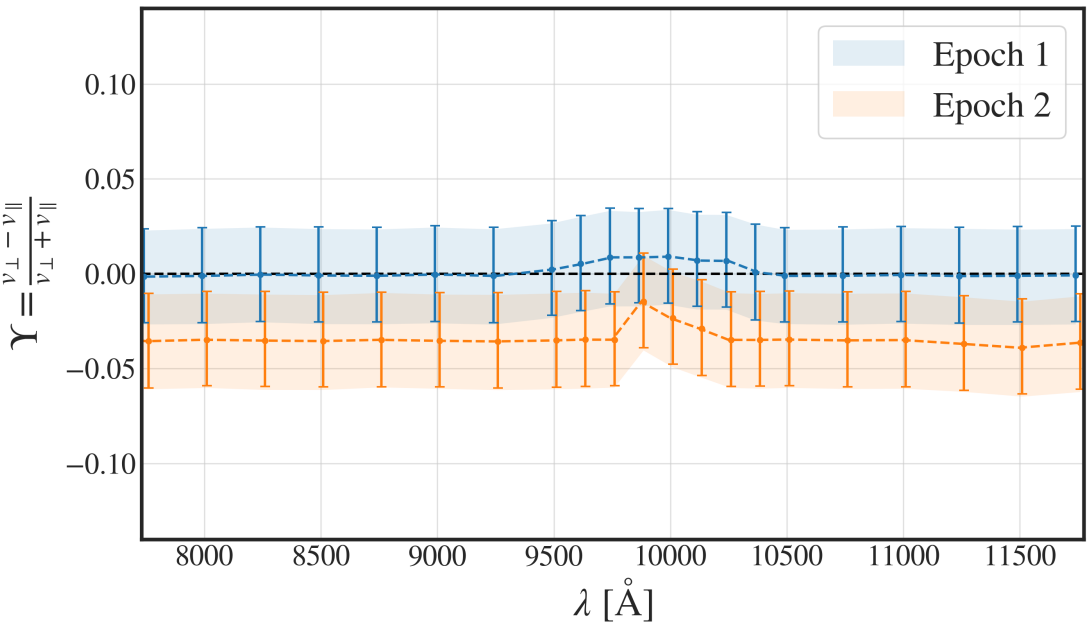

Figure 23: **Shift in asymmetry index for varying central wavelengths of additional P Cygni line** For no wavelengths do we observe a large shift contradicting sphericity, but a slight bias is present when the novel P Cygni feature is near but blueward of the Sr^+-lines.

extent which may alter our conclusion on sphericity. Fundamentally, the spectra are observationally well described by our simple prescription and do not require additional lines. While one can increase the complexity with a multitude of lines, a blend of lines conspiring to make an aspherical geometry look spherical is unlikely given the consistency in distance across multiple epochs. This would require, that despite the relative strength of lines varying with depth, densities and temperatures, these lines are still well-described by a singular P Cygni feature, which is 1) coherently shifted in wavelength and 2) receding deeper within the ejecta at exactly the rate predicted by the blackbody continuum.

4.1.5 Sr^+ - an accurate indicator of photospheric velocity?

A critical assumption for any determined distance or asphericity is that the Sr^+ lines are an accurate indicator of the photospheric velocity. This assumption is validated observationally in three separate respects.

Firstly, the observed line forming region continuously recedes deeper into the substructures over time, which is why the distance remains consistent across multiple epochs. If Sr^+ was detached from the photosphere, then as the photosphere recedes deeper into the substructures, the difference in velocity between the line forming region and the photosphere would become increasingly discrepant.

Secondly, while a high optical depth of a line may detach it from the photosphere, the optical depth of Sr^+ lines over all epochs analysed is moderate, yielding maximally a 20% reduction in flux with $\tau < 1$. At these moderate optical depths the P Cygni model is expected to trace the photospheric position [67].

Lastly, fitting the previously mentioned other P Cygni feature at $\sim 0.75\mu$m with the same prescription of the Elementary Supernova model [77] would yield a similar velocity as the Sr^+ lines (as detailed in Fig. 19). Note, there is as-of-yet no known or definitive spectral identification of this line, so the fit includes a free central wavelength, which while being constrained from the emission parts of the P Cygni does assume the spectral origin can be approximated by a singular line. Crucially, the constraint from this entirely independent line again supports the validity of velocities derived from Sr^+.

4.2 Advantages of EPM for Kilonovae Applications

Ultimately, kilonovae have provided remarkable apt terrain for the mathematical framework of EPM, yielding tight self-consistent constraints across multiple epochs and being in good agreement with independent distance estimates. However, this unambiguous constraint across epochs and lines, was not the generic expectation of the author nor indeed observed in the class of objects, Type II-Plateau supernovae, for which EPM has historically been most applied. In the following, we therefore deliberate on the

unique conditions of kilonovae, which caused these remarkable constraints.

1. The gravitational wave detection yields an immediate independent measure of the time of the merger. In contrast, SNe detections require fitting over multiple epochs to determine the precise time of the explosion. This not only removes an ill-constrained free parameter from the fit, it also directly allows us to measure distances from a single spectrum and test self-consistency.

2. The rapid follow-up and detailed spectroscopy allow a temporal examination of the evolving ejected material. It critically allows an examination in early phases where the complexity of lines is minimal and the blackbody spectrum provides a valid description.

3. The overall velocity of the ejected material is large, $v \approx 0.3c$, which results in a P Cygni profile spanning hundreds of nm's. This means that we have the detailed spectral information to derive the properties of the line profile. In contrast for supernovae the ratio of velocity-uncertainty to the total velocity is far larger, simply because the ejecta is expanding far less rapidly.

4. The unique elementary composition of r-process elements and the low number of electrons per unit mass implies that electron scattering is negligible. In contrast, for supernovae, the dominance of electron scattering requires invoking large dilution or correction factors.

5. We also note that kilonova occur in less dusty environments than core collapse supernovae, so the extinction corrections are typically small.

In conjunction, these unique observational and physical conditions provide a far tighter constraint for kilonovae than previously attainable for supernovae.

4.3 Potential physical causes of sphericity

With robust observational indications of spherical symmetry in the ejected photosphere of kilonovae, we now once again turn to the physical interpretations for our models of neutron-star mergers.

As mentioned in Sec. 1.5, sphericity in density and composition is not an expected outcome of hydrodynamical merger models. Further complicating for our interpretations of hydrodynamical models, is the expectation that ejecta at different depths may be ejected by different mass ejection channels. However, we observe a seemingly persistent near spherical symmetry over several early epochs. This consistency makes any coincidental model where sphericity is produced by matching different ejection channels unlikely, as this would not be a robust feature over a large range of velocities. Lastly, the absorption line shape constraints also suggest that the Sr opacity (not just the continuum opacity) is spherically symmetric. This further indicates that a coincidence scenario where a highly oblate density distribution is matched by a largely prolate specific opacity remains unlikely.

Nevertheless, there remain several potential physical mechanisms which could be invoked to explain the high degree of sphericity. For instance a large injection of energy immediately after the merger would smooth out the density [33]. However, the energetics required seem to be in excess of anything expected by radioactive heating so one would need to invoke more exotic physics (for instance the energetics from magnetic re-connection). One could also have an anisotropic injection of energy with a relativistic wind blowing out from the central remnant. For instance, for remnants with large magnetic fields the rotational energy of the system can be extracted and dissipated into the out-flowing wind. This process is called magnetar spindown for highly magnetic neutron stars [5, 78] or the Blandford-Znajek process for black holes [79]. In both cases large amounts of energy could theoretically within seconds be deposited in a rapidly expanding relativistic wind, which sets the geometry of the outer layers.

Ultimately, the remarkably high degree of sphericity suggests some unknown and physical mechanisms must homogenize and sphericalise the ejected matter. Thus, hinting at potentially exciting unknown physics within the kilonova environment, but for this thesis any interpretation of the origin of sphericity is merely speculative.

5 Conclusion

In this thesis, we have used the expanding photospheres method to probe the geometry of the kilonova AT2017gfo. Across early epochs, we observe a high consistency between the cross-sectional radius of the blackbody and the velocity of the Sr^+ lines. Combining line shape constraints with the known inclination angle from radio measurements yields a similar and consistent constraint. Thus, both frameworks suggest that the kilonova ejecta is expanding in a spherically symmetrical manner.

This presents a challenge to the still ill-constrained and diverse suite of hydrodynamical merger models, which may hint at unique energetics within the explosion. However, this spherical geometry also represents an opportunity, as the expanding photospheres method may provide a unique, statistically tight and remarkably robust measure of luminosity distances to kilonovae. Indeed, the distances derived within this thesis for AT2017gfo is in excellent agreement with numerous earlier independent estimates including gravitational waves, surface brightness fluctuations and the fundamental plane. This novel framework for measuring distances may also provide a local probe on the Hubble constant, which is entirely independent of the cosmic distance ladder. Ultimately, the synergy of different observational probes and the unique physical environment, make kilonovae apt terrain for such analysis.

Furthermore, in the process of exploring the geometry of expansion, we have discovered new avenues for future research. Firstly, we have found a novel P Cygni profile of unknown spectral origin at 0.75μm in epoch 4 and 5. The spectral information (especially the velocity stratification) of the line is interesting as it provides independent probes of geometry in later epochs, while a future spectral identification is exciting as it may improve our understanding on the composition and r-process synthesis occurring in kilonovae. Secondly, we have shown that the combination of rapid cooling and mildly relativistic velocities may modify the blackbody continuum. Inversely, these modifications to the continuum shape contains as-of-yet unexplored statistical constraining power for analysing the process of cooling or the rate of expansion from a

single high-resolution spectrum.

Ultimately, there remains a plethora of unexplored statistical information hiding within the spectral features of AT2017gfo. Determining what methods may unearth this hidden structure is of increasing relevance, especially considering the data expected from the growing sensitivity of gravitational wave detectors. Thus, it remains a matter of ongoing research to understand these spectral fingerprints and the stories they tell on this remarkable and spectacular domain of astrophysics.

References

[1] Hessels, J. W. T. *et al.* A Radio Pulsar Spinning at 716 Hz. *Science* **311**, 1901–1904 (2006). astro-ph/0601337.

[2] Reisenegger, A. Origin and evolution of neutron star magnetic fields. *arXiv e-prints* astro–ph/0307133 (2003). astro-ph/0307133.

[3] Metzger, B. D. Kilonovae. *Living Reviews in Relativity* **23**, 1 (2019). 1910.01617.

[4] Siegel, D. M. & Metzger, B. D. Three-Dimensional General-Relativistic Magnetohydrodynamic Simulations of Remnant Accretion Disks from Neutron Star Mergers: Outflows and r -Process Nucleosynthesis. **119**, 231102 (2017). 1705.05473.

[5] Thompson, T. A., Chang, P. & Quataert, E. Magnetar Spin-Down, Hyperenergetic Supernovae, and Gamma-Ray Bursts. **611**, 380–393 (2004). astro-ph/0401555.

[6] Metzger, B. D., Thompson, T. A. & Quataert, E. A Magnetar Origin for the Kilonova Ejecta in GW170817. **856**, 101 (2018). 1801.04286.

[7] Bovard, L. *et al.* r -process nucleosynthesis from matter ejected in binary neutron star mergers. **96**, 124005 (2017). 1709.09630.

[8] Bauswein, A., Goriely, S. & Janka, H. T. Systematics of Dynamical Mass Ejection, Nucleosynthesis, and Radioactively Powered Electromagnetic Signals from Neutron-star Mergers. **773**, 78 (2013). 1302.6530.

[9] Kasen, D., Metzger, B., Barnes, J., Quataert, E. & Ramirez-Ruiz, E. Origin of the heavy elements in binary neutron-star mergers from a gravitational-wave event. **551**, 80–84 (2017). 1710.05463.

[10] Abbott, B. P. *et al.* A gravitational-wave standard siren measurement of the Hubble constant. **551**, 85–88 (2017). 1710.05835.

[11] Abbott, B. P. *et al.* Gravitational Waves and Gamma-Rays from a Binary Neutron Star Merger: GW170817 and GRB 170817A. **848**, L13 (2017). 1710.05834.

[12] Siegel, D. M. GW170817 -the first observed neutron star merger and its kilonova: Implications for the astrophysical site of the r-process. *European Physical Journal A* **55**, 203 (2019). 1901.09044.

[13] Smartt, S. J. *et al.* A kilonova as the electromagnetic counterpart to a gravitational-wave source. **551**, 75–79 (2017). 1710.05841.

[14] Pian, E. *et al.* Spectroscopic identification of r-process nucleosynthesis in a double neutron-star merger. **551**, 67–70 (2017). 1710.05858.

[15] Bauswein, A., Just, O., Janka, H.-T. & Stergioulas, N. Neutron-star Radius Constraints from GW170817 and Future Detections. **850**, L34 (2017). 1710.06843.

[16] Watson, D. *et al.* Identification of strontium in the merger of two neutron stars. **574**, 497–500 (2019). 1910.10510.

[17] Riess, A. G. *et al.* A Comprehensive Measurement of the Local Value of the Hubble Constant with 1 km/s/Mpc Uncertainty from the Hubble Space Telescope and the SH0ES Team. *arXiv e-prints* arXiv:2112.04510 (2021). 2112.04510.

[18] Aghanim, N. *et al.* Planck 2018 results. VI. Cosmological parameters. *arXiv e-prints* arXiv:1807.06209 (2018). 1807.06209.

[19] Mörtsell, E., Goobar, A., Johansson, J. & Dhawan, S. Sensitivity of the Hubble Constant Determination to Cepheid Calibration. **933**, 212 (2022). 2105.11461.

[20] Wojtak, R. & Hjorth, J. Intrinsic tension in the supernova sector of the local Hubble constant measurement and its implications. **515**, 2790–2799 (2022). 2206.08160.

[21] Efstathiou, G. A Lockdown Perspective on the Hubble Tension (with comments from the SH0ES team). *arXiv e-prints* arXiv:2007.10716 (2020). 2007.10716.

[22] Steinhardt, C. L., Sneppen, A. & Sen, B. Effects of Supernova Redshift Uncertainties on the Determination of Cosmological Parameters. **902**, 14 (2020). 2005.07707.

[23] Rigault, M. *et al.* Strong dependence of Type Ia supernova standardization on the local specific star formation rate. **644**, A176 (2020). 1806.03849.

[24] Jones, D. O. *et al.* Should Type Ia Supernova Distances Be Corrected for Their Local Environments? **867**, 108 (2018). 1805.05911.

[25] Birrer, S. *et al.* TDCOSMO. IV. Hierarchical time-delay cosmography - joint inference of the Hubble constant and galaxy density profiles. **643**, A165 (2020). 2007.02941.

[26] Wong, K. C. *et al.* H0LiCOW - XIII. A 2.4 per cent measurement of H_0 from lensed quasars: 5.3σ tension between early- and late-Universe probes. **498**, 1420–1439 (2020). 1907.04869.

[27] Pesce, D. W. *et al.* The Megamaser Cosmology Project. XIII. Combined Hubble Constant Constraints. **891**, L1 (2020). 2001.09213.

[28] Chen, H.-Y., Fishbach, M. & Holz, D. E. A two per cent Hubble constant measurement from standard sirens within five years. **562**, 545–547 (2018). 1712.06531.

[29] Doctor, Z. Thunder and Lightning: Using Neutron-star Mergers as Simultaneous Standard Candles and Sirens to Measure Cosmological Parameters. **892**, L16 (2020). 1912.12218.

[30] Coughlin, M. W. *et al.* Standardizing kilonovae and their use as standard candles to measure the Hubble constant. *Physical Review Research* **2**, 022006 (2020). 1908.00889.

[31] Hotokezaka, K. *et al.* A Hubble constant measurement from superluminal motion of the jet in GW170817. *Nature Astronomy* **3**, 940–944 (2019). 1806.10596.

[32] Hotokezaka, K. *et al.* Mass ejection from the merger of binary neutron stars. **87**, 024001 (2013). 1212.0905.

[33] Rosswog, S., Korobkin, O., Arcones, A., Thielemann, F. K. & Piran, T. The long-term evolution of neutron star merger remnants - I. The impact of r-process nucleosynthesis. **439**, 744–756 (2014). 1307.2939.

[34] Kawaguchi, K., Fujibayashi, S., Shibata, M., Tanaka, M. & Wanajo, S. A Low-mass Binary Neutron Star: Long-term Ejecta Evolution and Kilonovae with Weak Blue Emission. **913**, 100 (2021). 2012.14711.

[35] Oechslin, R., Janka, H. T. & Marek, A. Relativistic neutron star merger simulations with non-zero temperature equations of state. I. Variation of binary parameters and equation of state. **467**, 395–409 (2007). astro-ph/0611047.

[36] Metzger, B. D. & Fernández, R. Red or blue? A potential kilonova imprint of the delay until black hole formation following a neutron star merger. **441**, 3444–3453 (2014). 1402.4803.

[37] Sekiguchi, Y., Kiuchi, K., Kyutoku, K., Shibata, M. & Taniguchi, K. Dynamical mass ejection from the merger of asymmetric binary neutron stars: Radiation-hydrodynamics study in general relativity. **93**, 124046 (2016). 1603.01918.

[38] Radice, D. *et al.* Binary Neutron Star Mergers: Mass Ejection, Electromagnetic Counterparts, and Nucleosynthesis. **869**, 130 (2018). 1809.11161.

[39] Just, O. *et al.* Dynamical ejecta of neutron star mergers with nucleonic weak processes - II: kilonova emission. **510**, 2820–2840 (2022). 2109.14617.

[40] Fernández, R. & Metzger, B. D. Electromagnetic Signatures of Neutron Star Mergers in the Advanced LIGO Era. *Annual Review of Nuclear and Particle Science* **66**, 23–45 (2016). 1512.05435.

[41] Perego, A. *et al.* Neutrino-driven winds from neutron star merger remnants. **443**, 3134–3156 (2014). 1405.6730.

[42] Just, O., Bauswein, A., Pulpillo, R. A., Goriely, S. & Janka, H.-T. Comprehensive nucleosynthesis analysis for ejecta of compact binary mergers. **448**, 541–567 (2015). 1406.2687.

[43] Wu, M.-R. & Tamborra, I. Fast neutrino conversions: Ubiquitous in compact binary merger remnants. **95**, 103007 (2017). 1701.06580.

[44] Kirshner, R. P. & Kwan, J. Distances to extragalactic supernovae. **193**, 27–36 (1974).

[45] Gall, C., Hjorth, J., Rosswog, S., Tanvir, N. R. & Levan, A. J. Lanthanides or Dust in Kilonovae: Lessons Learned from GW170817. **849**, L19 (2017). 1710.05863.

[46] Ghisellini, G. *Radiative Processes in High Energy Astrophysics*, vol. 873 (2013).

[47] Gall, E. E. E. *et al.* Applying the expanding photosphere and standardized candle methods to Type II-Plateau supernovae at cosmologically significant redshifts . The distance to SN 2013eq. **592**, A129 (2016). 1603.04730.

[48] Mooley, K. P. *et al.* Superluminal motion of a relativistic jet in the neutron-star merger GW170817. **561**, 355–359 (2018). 1806.09693.

[49] Drout, M. R. *et al.* Light curves of the neutron star merger GW170817/SSS17a: Implications for r-process nucleosynthesis. *Science* **358**, 1570–1574 (2017). 1710.05443.

[50] Shappee, B. J. *et al.* Early spectra of the gravitational wave source GW170817: Evolution of a neutron star merger. *Science* **358**, 1574–1578 (2017). 1710.05432.

[51] Sadun, A. C. & Sadun, L. A. Relativistic Dynamics of Expanding Sources. **185**, 21–36 (1991).

[52] Jeffery, D. J. & Branch, D. Analysis of Supernova Spectra. In Wheeler, J. C., Piran, T. & Weinberg, S. (eds.) *Supernovae, Jerusalem Winter School for Theoretical Physics*, vol. 6, 149 (1990).

[53] Tanvir, N. R. *et al.* The Emergence of a Lanthanide-rich Kilonova Following the Merger of Two Neutron Stars. **848**, L27 (2017). 1710.05455.

[54] Foreman-Mackey, D., Hogg, D. W., Lang, D. & Goodman, J. emcee: The MCMC Hammer. **125**, 306 (2013). 1202.3665.

[55] Newville, M. *et al.* Lmfit: Non-Linear Least-Square Minimization and Curve-Fitting for Python. Astrophysics Source Code Library, record ascl:1606.014 (2016). 1606.014.

[56] Cantiello, M. *et al.* A Precise Distance to the Host Galaxy of the Binary Neutron Star Merger GW170817 Using Surface Brightness Fluctuations. **854**, L31 (2018). 1801.06080.

[57] Hjorth, J. *et al.* The Distance to NGC 4993: The Host Galaxy of the Gravitational-wave Event GW170817. **848**, L31 (2017). 1710.05856.

[58] Howlett, C. & Davis, T. M. Standard siren speeds: improving velocities in gravitational-wave measurements of H_0. **492**, 3803–3815 (2020). 1909.00587.

[59] Mukherjee, S. *et al.* Velocity correction for Hubble constant measurements from standard sirens. **646**, A65 (2021). 1909.08627.

[60] Nicolaou, C., Lahav, O., Lemos, P., Hartley, W. & Braden, J. The impact of peculiar velocities on the estimation of the Hubble constant from gravitational wave standard sirens. **495**, 90–97 (2020). 1909.09609.

[61] Hoeflich, P., Wheeler, J. C., Hines, D. C. & Trammell, S. R. Analysis of the Polarization and Flux Spectra of SN 1993J. **459**, 307 (1996). astro-ph/9510031.

[62] Mooley, K. P., Anderson, J. & Lu, W. Optical superluminal motion measurement in the neutron-star merger GW170817. **610**, 273–276 (2022). 2210.06568.

[63] Covino, S. *et al.* The unpolarized macronova associated with the gravitational wave event GW 170817. *Nature Astronomy* **1**, 791–794 (2017). 1710.05849.

[64] Bulla, M. *et al.* The origin of polarization in kilonovae and the case of the gravitational-wave counterpart AT 2017gfo. *Nature Astronomy* **3**, 99–106 (2019). 1809.04078.

[65] Kim, A. G. & Linder, E. V. Complementarity of peculiar velocity surveys and redshift space distortions for testing gravity. **101**, 023516 (2020). 1911.09121.

[66] Abbott, B. P. *et al.* Prospects for observing and localizing gravitational-wave transients with Advanced LIGO, Advanced Virgo and KAGRA. *Living Reviews in Relativity* **21**, 3 (2018). 1304.0670.

[67] Sim, S. A. Spectra of Supernovae During the Photospheric Phase. In Alsabti, A. W. & Murdin, P. (eds.) *Handbook of Supernovae*, 769 (2017).

[68] Domoto, N. *et al.* Lanthanide Features in Near-infrared Spectra of Kilonovae. *arXiv e-prints* arXiv:2206.04232 (2022). 2206.04232.

[69] Ball, L., Campbell-Wilson, D. & Staveley-Smith, L. Travel-time delays in radio supernova remnant 1987 A. **276**, 944–946 (1995).

[70] Hershkowitz, S., Linder, E. & Wagoner, R. V. Spectral Flux from Low-Density Photospheres: Approximate Results. **303**, 800 (1986).

[71] Vogl, C., Sim, S. A., Noebauer, U. M., Kerzendorf, W. E. & Hillebrandt, W. Spectral modeling of type II supernovae. I. Dilution factors. **621**, A29 (2019). 1811.02543.

[72] Eastman, R. G., Schmidt, B. P. & Kirshner, R. The Atmospheres of Type II Supernovae and the Expanding Photosphere Method. **466**, 911 (1996).

[73] Dessart, L. & Hillier, D. J. Distance determinations using type II supernovae and the expanding photosphere method. **439**, 671–685 (2005). astro-ph/0505465.

[74] Dessart, L. *et al.* Radiative-transfer models for supernovae IIb/Ib/Ic from binary-star progenitors. **453**, 2189–2213 (2015). 1507.07783.

[75] Kasen, D., Badnell, N. R. & Barnes, J. Opacities and Spectra of the r-process Ejecta from Neutron Star Mergers. **774**, 25 (2013). 1303.5788.

[76] Hershkowitz, S., Linder, E. & Wagoner, R. V. Spectral Flux from Low-Density Photospheres: Approximate Results. **303**, 800 (1986).

[77] Noebauer, U. pcygni_profile. https://github.com/unoebauer/public-astro-tools (2018).

[78] Metzger, B. D., Thompson, T. A. & Quataert, E. A Magnetar Origin for the Kilonova Ejecta in GW170817. **856**, 101 (2018). 1801.04286.

[79] Blandford, R. D. & Znajek, R. L. Electromagnetic extraction of energy from Kerr black holes. **179**, 433–456 (1977).

Appendix

Example Posterior Distributions of Parameters

Here we illustrate the posterior distribution of key parameters for epochs 2, 3 and 4. The parameters shown are the blackbody temperature, T, the blackbody normalisation, $N \cdot 10^{30}$, the photospheric velocity, v_{phot}, the maximum ejecta velocity, v_{max}

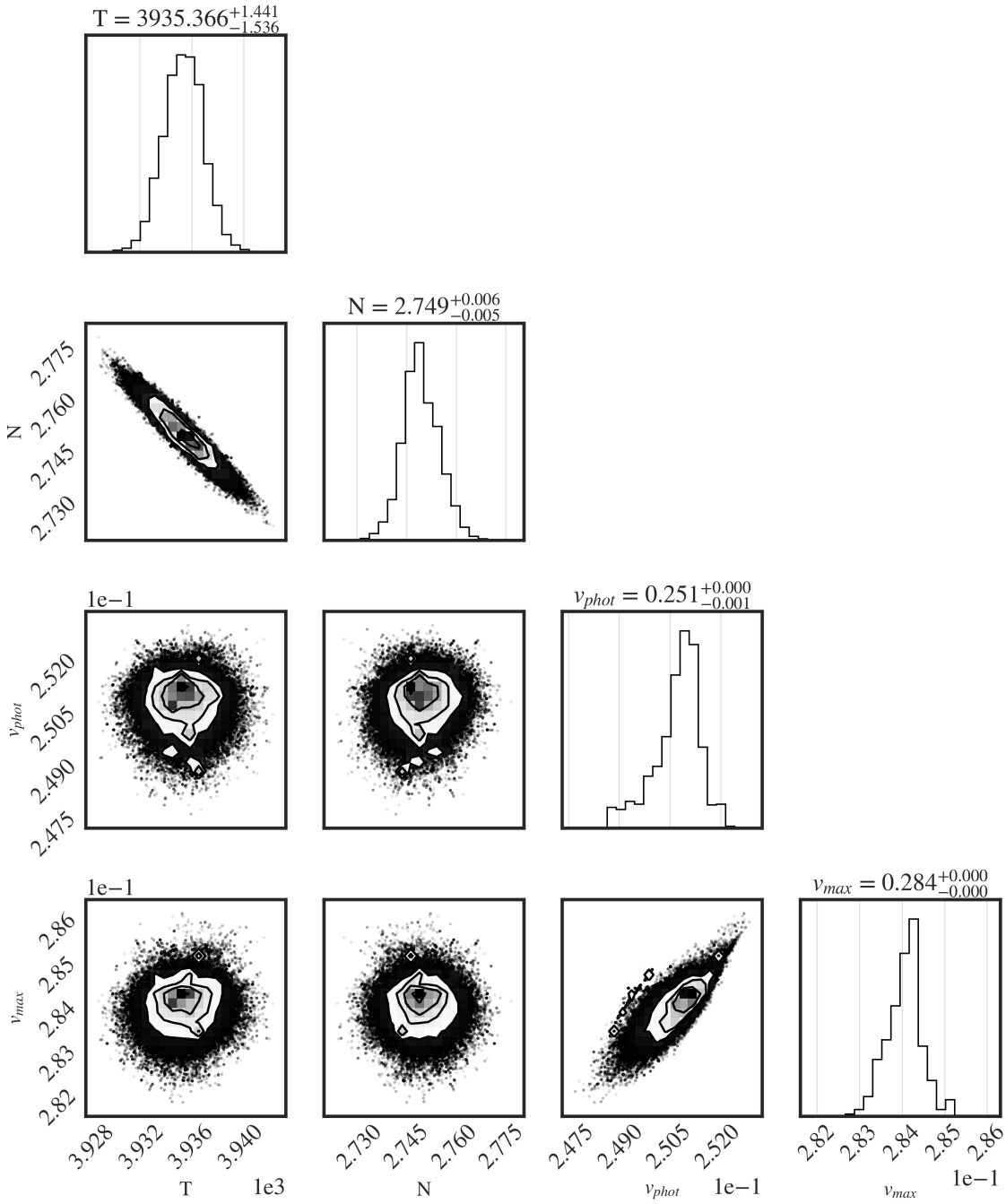

Figure 24: Corner plot indicating posterior distribution of several key parameters for second epoch. The posterior distribution is convex with singular global minimum.

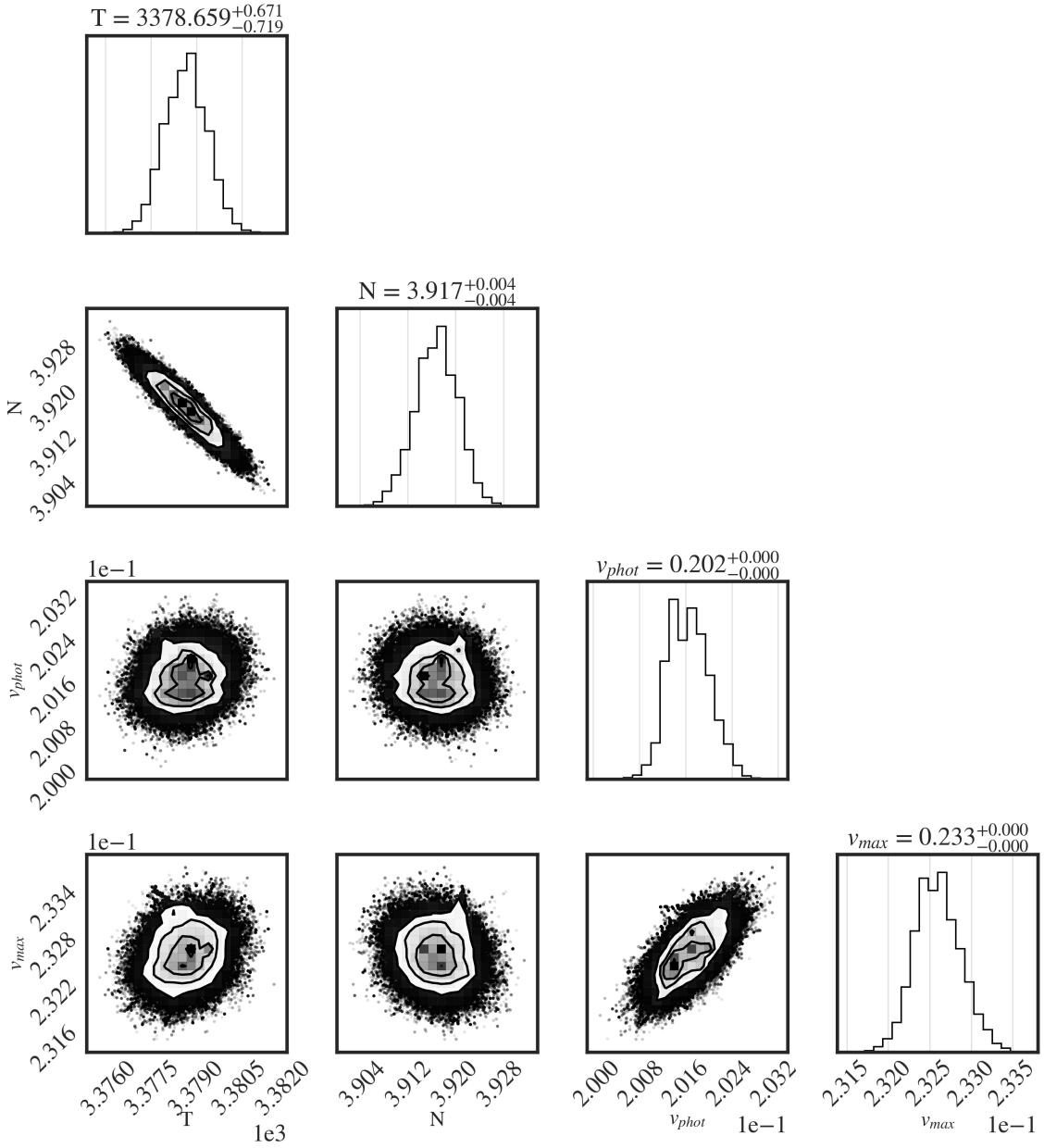

Figure 25: Corner plot indicating posterior distribution of several key parameters for third epoch. The posterior distribution is convex with singular global minimum.

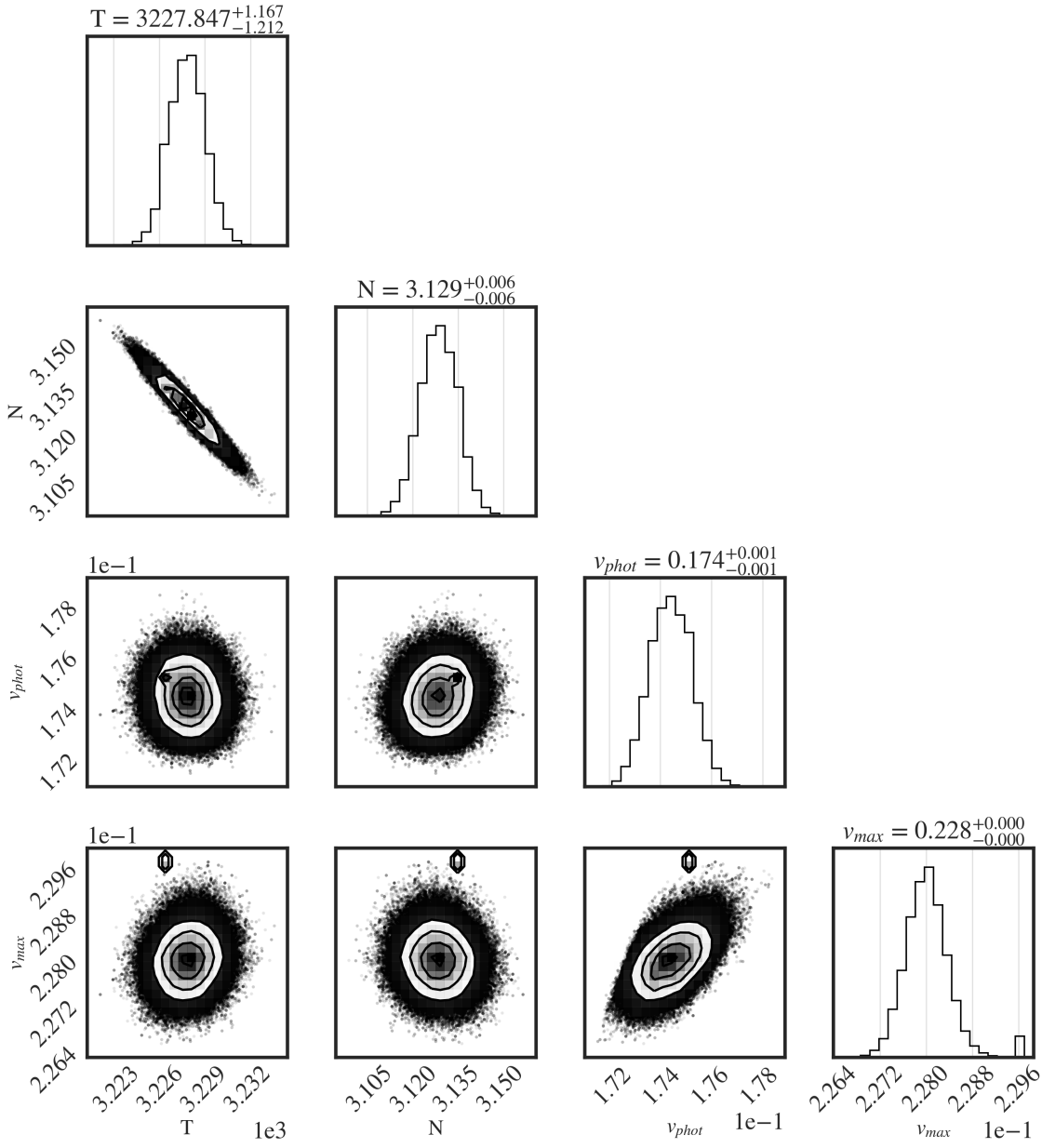

Figure 26: Corner plot indicating posterior distribution of several key parameters for fourth epoch. The posterior distribution is convex with singular global minimum.